



## Vertical distributions of blooming cyanobacteria populations in a freshwater lake from LIDAR observations



Timothy S. Moore<sup>a,\*</sup>, James H. Churnside<sup>b</sup>, James M. Sullivan<sup>c</sup>, Michael S. Twardowski<sup>c</sup>, Aditya R. Nayak<sup>c,d</sup>, Malcolm N. McFarland<sup>c</sup>, Nicole D. Stockley<sup>c</sup>, Richard W. Gould<sup>g</sup>, Thomas H. Johengen<sup>e</sup>, Steven A. Ruberg<sup>f</sup>

<sup>a</sup> University of New Hampshire, Durham, NH, USA

<sup>b</sup> NOAA Earth System Research Laboratory, Boulder, CO, USA

<sup>c</sup> Harbor Branch Oceanographic Institute, Florida Atlantic University, Fort Pierce, FL, USA

<sup>d</sup> Department of Ocean and Mechanical Engineering, Florida Atlantic University, Boca Raton, FL, USA

<sup>e</sup> Cooperative Institute for Limnology and Ecosystems Research, University of Michigan, Ann Arbor, MI, USA

<sup>f</sup> NOAA Great Lakes Environmental Research Laboratory, Ann Arbor, MI, USA

<sup>g</sup> Bio-Optical/Physical Processes and Remote Sensing Section, Naval Research Laboratory, Code 7331, Stennis Space Center, MS, USA

### ARTICLE INFO

#### Keywords:

Remote sensing  
Harmful algal blooms  
LIDAR  
Cyanobacteria  
Species distributions  
Holography

### ABSTRACT

The vertical distributions of freshwater cyanobacteria populations are important to plankton community structure, ecology and for influencing water column optical properties relevant to remote sensing. In August of 2014, we examined the vertical structure of a cyanobacteria bloom across the western basin of Lake Erie with new technologies, including LIDAR and a digital holographic system. In addition, vertical profiles of environmental and optical properties were made. The active LIDAR penetrated the water column, and provided a detailed picture of the particle distribution for the whole water column. The holographic system provided digital images processed for particle size, count and identification of *Microcystis* and *Planktothrix* - the two main cyanobacteria genera that were present. The correlations between the LIDAR backscatter intensity and the cyanobacteria cell counts from holography averaged to 0.53 and ranged from −0.13 to 0.96 based on nearest matchups. The vertical structure of the overall cyanobacteria population was influenced by wind speed, and to a lesser degree the solar heating of surface waters. On a more detailed level, *Microcystis* populations were consistently nearer to the surface relative to *Planktothrix*. Pigments from surface samples revealed a higher degree of photoprotection for *Planktothrix*-dominated communities. The vertical distributions of the cyanobacteria genera were related to light intensity in the water column and known tolerances and/or preferences for each genus. Vertical profiles of optical properties supported the patterns seen in the LIDAR and holographic data, and had direct implications on the exiting light field. These combined data provide a unique view into the natural variations in spatial (vertical and horizontal) distribution patterns of cyanobacteria and resulting impacts on remote sensing detection and associated interpretations, and demonstrate the potential for these technologies to observe cyanobacteria in lake environments.

### 1. Introduction

Cyanobacteria inhabit lake systems worldwide (Harke et al., 2016), and have a long evolutionary history resulting in a diversity of ecological strategies and traits from long-term adaptations (Uyeda et al., 2016; Blank, 2013; Sánchez-Baracaldo et al., 2005). One trait shared across a large number of cyanobacteria genera is the ability to regulate buoyancy with the aid of gas vesicles (Carey et al., 2012; Walsby, 1994). The role of buoyancy in cyanobacteria ecology has long been a

research topic and viewed as an important factor for ecological success (Harke et al., 2016; Walsby et al., 1997; Ibelings et al., 1994; Humphries and Lyne, 1988). This capability gives an organism an advantage for accessing light and nutrient resources for optimizing photosynthesis and growth.

Buoyancy regulation in gas-vacuolate cyanobacteria is a function of overall cell density, largely derived from the balance between intracellular gas vesicle volume and the amount of other cellular components, especially carbohydrates (Visser et al., 1997; Oliver, 1994).

\* Corresponding author.

E-mail address: [timothy.moore@unh.edu](mailto:timothy.moore@unh.edu) (T.S. Moore).

Gas vesicles can be synthesized or collapsed by cells to increase or decrease buoyancy, respectively (Oliver, 1994). Cell ballast change through carbohydrate content is another mechanism to regulate buoyancy. Carbohydrate content can fluctuate rapidly in cells, usually on shorter time scales than gas vesicle changes (Oliver, 1994). By adjusting these compartments, cells and larger colonial aggregates can alter buoyancy to migrate upwards or downwards in the water column with rates of several meters per hour (Visser et al., 1997).

There are multiple environmental factors that influence buoyancy regulation in cyanobacteria, led by light level exposure and external nutrient levels (Walsby et al., 2004; Oliver, 1994; Konopka, 1989). Buoyancy responses to changing light conditions have been reported in laboratory experiments and in natural settings. In laboratory experiments of *Planktothrix* populations, a genus with filamentous morphologies, dark-adapted cells lost buoyancy when exposed to increased light levels, and increased buoyancy in lower light intensities (e.g., Visser et al., 1997; Oliver and Walsby, 1984; Walsby and Booker, 1980). Across different natural settings, *Planktothrix* populations have been observed to rise and/or sink in response to light exposure (Walsby et al., 2004; Davis et al., 2003; Kromkamp and Walsby, 1990). In these cases, the cyanobacteria populations maintained neutral buoyancy during stratified periods; that is, vertical position was maintained at depth without escaping to the surface or to the bottom outside the preferred zone. Based on these behavioral patterns to light, *Planktothrix* are considered shade-adapted (Walsby et al., 2004; Davis et al., 2003; Halvstedt et al., 2007).

The degree to which cells respond to light in terms of buoyancy regulation varies between genera, species and even within species depending on physiological state (Oliver, 1994). As a result, differing light tolerances/preferences can create niche separation along vertical gradients allowing for co-existence. This has been observed with different *Planktothrix* species (Kokocinski et al., 2010; Davis et al., 2003), and marine cyanobacteria (Stomp et al., 2007). *Microcystis* is another commonly found cyanobacteria genus and has been studied for decades, with its ecological success linked to buoyancy regulation (Paerl and Otten, 2013; Davis et al., 2003; Paerl et al., 1985). *Microcystis* is well known for colony formation from aggregating cells and forming surface blooms during calm wind periods. Colonial aggregates are believed to enhance vertical migration, and can promote excessive or 'overbuoyancy' (Oliver, 1994; Paerl et al., 1983) leading to surface scum formation. Studies by Paerl et al. (1985, 1983) elaborated on the ability of *Microcystis* surface blooms to withstand the high light environment. The studies determined that not only did photoprotective pigments (e.g., zeaxanthin) shield cells from otherwise dangerous excessive light, the photosynthetic efficiencies often increased in surface blooms of *Microcystis*. Given their widespread distribution around the globe and long geologic history, it is an aspect of their evolutionary success that enables *Microcystis* to not only withstand but in certain cases thrive at high light, giving them a competitive advantage under those conditions and potentially shading out competitors (Paerl et al., 1985).

The vertical distributions of cyanobacteria have implications for remote sensing applications. Gas-vacuolate cyanobacteria have high scatter and backscatter efficiency (Matthews and Bernard, 2013; Moore et al., 2017) which elevates light backscattered out of the water the nearer they are to the surface. Kutser (2004) describes three states of cyanobacteria vertical distributions in the context of remote sensing. The states include vertically uniform distributions, near-surface distributions, and floating scums - each of which has a different impact on the spectral remote sensing reflectance ( $R_{rs}(\lambda)$ ), the quantity that is detected by radiometers including those on satellites. The  $R_{rs}(\lambda)$  is proportional to the light scattered back out of the water from a layer extending from the surface to a variable depth, which is a function of the attenuation coefficient of light and wavelength (Kirk, 1994). This depth can be 1 m or less in dense, near-surface cyanobacteria blooms (Kutser, 2004). In these cases,  $R_{rs}(\lambda)$  is enhanced to the extreme point of resembling land foliage. Conversely, if a cyanobacteria population is

concentrated in a deeper sub-surface layer, they may be below the detection depth of satellite sensors, and may contribute weakly or not at all to  $R_{rs}(\lambda)$ . This type of distribution does not fit into one of the three states, although it has been observed in nature (e.g., Davis et al., 2003; Walsby et al., 2004). Knowing the state or vertical distribution of cyanobacteria populations in natural environments improves the understanding of cyanobacteria ecology and the interpretations of the remote sensing observations. These two aspects are important to assessing and determining lake water quality attributes.

Vertical profile measurements of optical properties in freshwater lakes for remote sensing studies are scarce (see Xue et al., 2017 and references therein). Most remote sensing studies of cyanobacteria blooms focus on surface conditions. However, recent modeling studies have investigated the impacts of gas-vacuolate cyanobacteria on  $R_{rs}(\lambda)$  (Xue et al., 2017; Matthews and Bernard, 2013; Kutser et al., 2008; Metsamaa et al., 2006). These studies revealed the dependencies of the  $R_{rs}(\lambda)$  on the vertical structure of biomass and their associated inherent optical properties (IOPs) such as the absorption and backscatter coefficients. A general conclusion from these studies is that non-uniform vertical structure is a complication for remote sensing algorithms used for quantifying cyanobacteria biomass.

We previously reported on the horizontal distributions of surface optical properties in western Lake Erie during a cyanobacteria bloom (Moore et al., 2017), and identified two genera of cyanobacteria dominating the microbial community - *Microcystis* and *Planktothrix*. During our field sampling in August 2014, another experiment led by the Naval Research Laboratory (NRL) was sampling the same area with similar optical packages, and measuring for a suite of surface pigments. In addition, a Light Detection and Ranging (LIDAR) instrument, developed in-house at the National Oceanic and Atmospheric Administration (NOAA), was flown on-board a Twin Otter aircraft taking measurements over the western and central basins of Lake Erie. The LIDAR instrument is able to detect vertical profiles of optical back-scattering from particles (e.g., cyanobacteria cells and colonies, suspended sediments) in surface waters, and is the only remote sensing technique that can profile the upper water column from above the surface (Churnside, 2014). Comparisons of LIDAR returns with in water measurements of optical backscattering have shown good agreement (Lee et al., 2013; Churnside et al., 2017). The LIDAR can measure particle distributions with a vertical resolution of less than 1 m and a horizontal resolution of 5 to 15 m (Churnside and Donaghay, 2009; Churnside, 2015). In clear oceanic water, these profiles can reach 50 m in depth. During the study period, the penetration was less in Lake Erie because of higher density of particles, but the full water column was measured in many places of the western basin.

### 1.1. Objectives

The field and aircraft measurements collected during August of 2014 from this location provide a unique data set to assess the vertical distributions of cyanobacteria populations in natural settings and their impacts on remote sensing. The goals of this study are to 1) examine the associations between the vertical distributions of particle fields from LIDAR data and vertical distributions of optical properties and cyanobacteria counts measured in Lake Erie; and 2) to assess these findings in the context of cyanobacteria ecology and impacts on bio-optical algorithms used in remote sensing applications.

## 2. Methodology

### 2.1. Study area

Lake Erie comprises three connected basins, distinguished by bathymetry and other natural features - the western, central and eastern basins. Observations from aircraft and direct sampling from this study were made in the western basin, and the western edge of the central

basin. Mean flow is from west to east, and thus water flows from the western basin to the central basin. The mean residence time of water in the western basin is 50 days (Millie et al., 2009). The two largest and most important rivers flowing into the western basin are the Maumee River, entering the basin in the southwest corner (Maumee Bay) through the city of Toledo, and the Detroit River entering the basin in the northwest corner. The Maumee River watershed is dominated by agricultural land (Jooosse and Baker, 2011), and supplies much of the nutrient load to the western basin (Stumpf et al., 2012; Michalak et al., 2013; IJC, 2014), despite the Detroit River delivering over 80% of the annual basin-wide discharge by volume. The Detroit River waters are poorer in nutrient content, and are optically different from waters to the south in Maumee Bay (Moore et al., 2017). The western basin transitions to the deeper central basin in an area populated by islands known as the Lake Erie Islands, with the two largest comprising Pelee Island (to the north) and Kellys Island (to the south). West of these islands are three smaller islands called North, Middle and South Bass Islands. Other smaller islands are also within this island vicinity. Sandusky Bay is a shallow, enclosed water body receiving water from the Sandusky River, and discharges into the southwestern central basin and also plays a role as a source of cyanobacteria to Lake Erie (Davis et al., 2015; Kane et al., 2014).

To aid in understanding patterns in the data, we have further identified nine sub-regions within the overall study area corresponding to geographic and hydrographic features (Fig. 1). Not all of these regions were directly sampled in the field, but all were observed with the LIDAR. These areas are: 1 - southeastern western basin; 2 - Detroit River plume front (a transition region between the Detroit River and Maumee Bay water); 3 - Detroit River (a quasi-permanent hydrographic feature in the northwest corner); 4 - Maumee Bay (the shallowest part of the basin that directly receives Maumee River discharge); 5 - Islands West (an area to the west of the islands in the western basin); 6 - Islands Central (a transition region encompassing the islands); 7 - Islands East (an area to the east of the islands extending into the deeper central basin); 8 - Islands Southeast (an area in the central basin outside the entrance of Sandusky Bay); 9 - Sandusky Bay. Maumee and Sandusky Bays were observed with LIDAR only. Echograms from these two areas (4 and 9) are contained in a supplement at the end of this manuscript.

## 2.2. Data sets

Field and aircraft data were collected between August 17, 2014 and August 28, 2014 (Table 1). The field data were derived from two separately conducted but simultaneous field surveys (Table 2). The first data set comprised 20 stations led by the University of New Hampshire (UNH), and included surface water discrete samples, vertical profiles of inherent optical properties (IOPs), above-water  $R_{rs}(\lambda)$ , and digital holographic profiles. The second data set was generated from a simultaneous field survey led by the Naval Research Laboratory (NRL) and comprised vertical IOP profiles ( $N = 11$ ),  $R_{rs}(\lambda)$  and surface water discrete samples for pigments. Not all stations had the same suite of measurements. These are indicated on the map in Fig. 1.

### 2.2.1. Discrete measurements

Discrete measurements of surface water quality parameters for the UNH data set included suspended particulate matter (SPM), chlorophyll-a concentration ( $Chl-a$ ), phycocyanin concentration (PC). The details of the processing are contained in Moore et al. (2017). We further determined volatile (organic) and non-volatile SPM by combusting filters for 4 h at 450 °C, cooling, and reweighing (APHA, 1998).

The NRL discrete data comprised surface water samples processed for high pressure liquid chromatography (HPLC). Some of these did not coincide with any IOP profiles. Thus, in addition to the 11 NRL stations with profiles, another 9 stations contained HPLC samples only (see Fig. 1). The HPLC data were processed with an Agilent RR1200 system, and extraction and pigment concentration followed the protocol

detailed in Heukelem and Thomas (2001). A set of pigments were quantified, and included but not limited to total chlorophyll-a and zeaxanthin. In our analysis, we only used these pigments, with zeaxanthin being a major photoprotective pigment found in cyanobacteria (Jeffrey et al., 1997), including *Microcystis* and *Planktothrix*. We used these two pigments to quantify the degree of internal photoprotection in the surface algal populations across the study region.

### 2.2.2. IOP vertical profiles

Vertical profiles of optical and hydrographic properties from the UNH data set were collected at 14 stations. The vertical profiling system included a WET Labs (Philomath, OR) ac-9 measuring absorption and attenuation at 9 wavelengths: 412, 440, 488, 510, 532, 555, 650, 676 and 715 nm, backscattering meters (WET Labs ECO-VSF, ECO-BB3, and ECO-BB9 sensors) and a SeaBird (Bellevue, WA) SBE49 CTD. The ac-9 was calibrated with Milli-Q ultrapure water, and absorption  $a(\lambda)$  was corrected for scattering effects using the proportional method of Zaneveld et al. (1994). Data were corrected for temperature and salinity effects using the coefficients of Twardowski et al. (1999) using the CTD data. Two profiles were made at each station. The first profile was taken without any filters to derive total absorption ( $a_t$ ). A 0.2  $\mu\text{M}$  filter was fitted on the ac-9 for the second profile to derive dissolved absorption ( $a_d$ ). From the two profiles, particulate absorption ( $a_p$ ) was derived by subtracting water ( $a_w$ ) and dissolved absorption from total absorption. Of these, we report only on the particulate absorption in Section 3. Particulate scattering  $b_p(\lambda)$  was derived from the ac-9 as the difference between attenuation  $c(\lambda)$  and absorption  $a(\lambda)$ . We further derived the particle backscatter ratio -  $\tilde{b}_{bp}$  - as the particle backscatter coefficient ( $b_{bp}(\lambda)$ ) divided by  $b_p(\lambda)$ . This parameter provides insight into the nature of the particle composition, especially in detecting the presence of gas-vacuolate cyanobacteria (Moore et al., 2017). All data were averaged into 0.5 m depth bins. Further details of the package and data processing are contained in Moore et al. (2017).

For the NRL data set, 11 stations were sampled with a vertical profiling package that included dual WET Labs ac-9 systems - one equipped with a 0.2  $\mu\text{M}$  filter and one for non-filtered water - measuring absorption and attenuation at the same wavelengths as above. Processing of the ac-9 data followed the same processing protocol applied to the above ac-9 data. Further details are available on the NASA SeaBASS website (Gould, 2014).

### 2.2.3. LIDAR data

Between August 17 through August 28, 2014, over 50 LIDAR tracks were flown over Lake Erie. The LIDAR, developed in-house at NOAA, used linearly polarized light at a wavelength of 532 nm. The laser transmitter produced 100 mJ in 10 ns pulses at a rate of 30 Hz. The beam was expanded to 5 mrad, so the illuminated spot diameter depended on flight altitude. For the data reported here, the spot diameter was generally between 5 and 8.5 m, except for track T23, where it was 15 m. Two receiver telescopes collected the returns that were co-polarized and cross-polarized with respect to the transmitted light. Each channel used a photomultiplier tube as a detector, followed by a logarithmic amplifier and an eight bit digitizer with a 1 GHz sample rate. For this study, the cross-polarized channel was used, because it provides better sensitivity to large, irregularly shaped particles such as *Microcystis* and *Planktothrix* colonial aggregates. The reason for this sensitivity is that a co-polarized or unpolarized receiver is sensitive to light that is specularly reflected from the surface, scattered by spherical particles like bubbles in the water, and scattered by lake water. None of these components depolarize, so their contribution can mask the co-polarized scattering from the algal cells of interest. The most common effect would be an enhanced signal near the surface due to the specular reflection and bubbles near the surface. This enhanced signal might be mistaken for a surface algal layer unless the cross-polarized return is used. The system was not calibrated to provide cell counts, but all data are presented on the same relative scale.

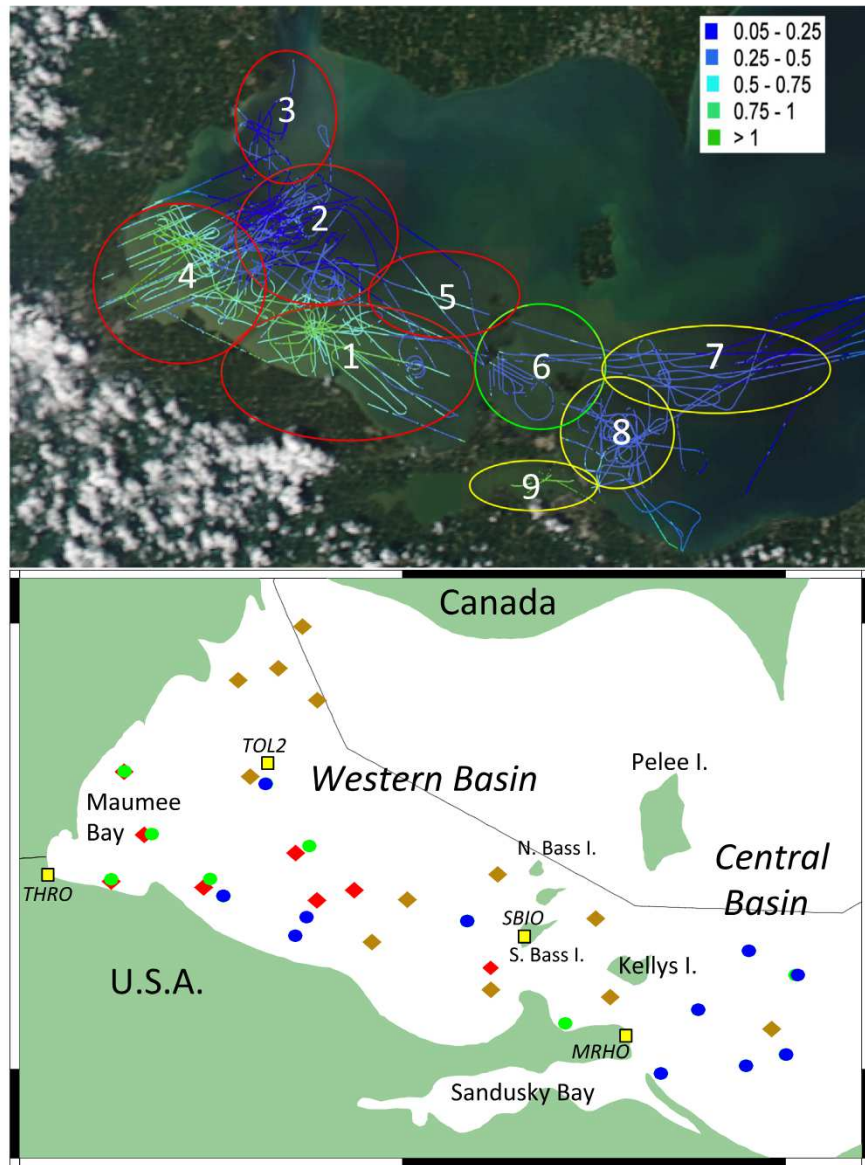


**Fig. 1.** Top: Map of LIDAR flight tracks in August, 2014, color coded by LIDAR attenuation coefficient in  $\text{m}^{-1}$ , superimposed on the MODIS true-color image from August 25. Sub-region identification scheme for LIDAR track data: 1 - southeastern western basin; 2 - Detroit River plume front; 3 - Detroit River; 4 - Maumee Bay; 5 - islands west; 6 - islands central; 7 - islands east; 8 - islands southeast; 9 - Sandusky Bay. Bottom: locations of discrete stations. Station legend: diamonds - UNH data; circles - NRL data; brown - Holocam, IOPs, SPM,  $R_{rs}$ ; red - IOP, SPM blue -  $R_{rs}$ , IOP, HPLC; green - HPLC only; yellow squares: wind stations - Toledo Light 2 (TOL2), NOS Toledo (THRO), South Bass Island (SBIO) and Marblehead (MRHO). (For interpretation of the references to color in this figure legend, the reader is referred to the web version of this article.)

Processing of the LIDAR data involved several steps. First, segments of the data were identified where the aircraft was flying straight and level. Then, the raw digitization levels for these segments were converted to photo-cathode current values using the measured system response. The surface was identified in each LIDAR return, and the depth of each subsurface sample calculated from the time difference between the surface and that sample. The exponential attenuation of the signal in water was estimated for each return using a linear regression to the logarithm of the return over the depth range of 2–4 m, and the data were corrected to remove the effects of attenuation. Finally, the data were multiplied by the square of aircraft altitude, so data taken at different altitudes can be compared directly.

Background level and system noise level were calculated as the mean and standard deviation of the last 100 samples of each shot. Background level was subtracted from each sample. Penetration depth was defined as the depth at which the signal first dropped to less than 3 times the system noise level. For all flights, the median penetration depth was 14 m, and the penetration depth was over 6 m for 90% of the data. This is consistent with penetration depths found in other turbid waters, such as Chesapeake Bay (Churnside et al., 2011). Data from below the calculated penetration depth were not used in the analysis to eliminate possible artifacts.

From the processing, cross-polarized attenuation, cross-polarized penetration depth and cross-polarized echograms were generated. We will be primarily showing the echograms from a number of tracks, which show along-track vertical distributions of particles. These have been smoothed in the vertical dimension by the finite laser pulse length, which corresponds to a sliding window of about 1 m. Some tracks were initiated with north-to-south or east-to-west orientation. In our subsequent figures, we mirror-reverse some echograms to match the orientation of the lake. All echograms were displayed to the same absolute color scale of 0–7.8  $\text{A m}^2$ , which corresponds to a LIDAR signal current of 0–7.8  $\mu\text{A}$  at a flight altitude of 1000 m. The intensity of the LIDAR signal current is directly proportional to the particle concentration, and thus the color is a reflection of particle concentration. Each x-axis is also on a dimensionless relative scale. Absolute distance and other track information (time, date, location) are contained in Table 3. In all cases, the data were inspected visually to ensure that the echograms were not influenced by reflections from the lake bottom.

### 2.3. Diffuse attenuation coefficient and optical depth

The diffuse attenuation coefficient at 490 nm,  $K_d490$ , was estimated from the IOP data based on Lee et al. (2005):

**Table 1**Matrix of *in situ* measurements and LIDAR track availability by area (see Fig. 1). Y = potential measurement availability.

Area	Type	8/17	8/18	8/19	8/20	8/21	8/22	8/23	8/24	8/28
1 SE Western Basin	LIDAR	Y	Y	Y					Y	
	IOP			Y	Y	Y	Y			
	HOLOCAM				Y	Y	Y			
2 Detroit River front	LIDAR	Y							Y	
	IOP									
	HOLOCAM									
3 Detroit River	LIDAR			Y						
	IOP				Y					
	HOLOCAM					Y				
4 Maumee Bay	LIDAR		Y	Y						
	IOP		Y							
	HOLOCAM									
5 Islands West	LIDAR	Y		Y			Y			
	IOP				Y					
	HOLOCAM					Y				
6 Islands Central	LIDAR		Y			Y				
	IOP				Y					
	HOLOCAM					Y				
7 Islands East	LIDAR					Y	Y	Y	Y	
	IOP					Y				
	HOLOCAM									
8 Islands Southeast	LIDAR		Y	Y			Y			
	IOP				Y					
	HOLOCAM					Y				
9 Sandusky Bay	LIDAR									Y
	IOP									
	HOLOCAM									

$$K_d(490) = (1 + .005 * \text{solz}) * a + 4.18 * (1 - 0.52 * \exp(-10.8 * a)) * b_b \quad (1)$$

where  $\text{solz}$  is the solar zenith angle,  $a$  is the total absorption at 490 nm, and  $b_b$  is the total backscatter at 490 nm. The optical depth at which 10% of the light remains is calculated as:

$$Z_{10\%} = \frac{2.3}{K_d(490)} \quad (2)$$

### 2.3.1. HOLOCAM particle count and cell identification

Phytoplankton populations were identified and counted using the HOLOCAM, an *in situ* holographic imaging system (Twardowski et al., 2016; Zamankhan et al., 2016; Nayak et al., 2018). Briefly, digital holography involves illuminating a region of interest (sample volume) with a coherent beam of light (e.g., laser beam). The diffraction patterns that are a result of the interference between light scattered by particles in the volume, and the undisturbed portion of the laser beam, are recorded on an imaging device. Numerical schemes are then used to reconstruct the hologram in 2-D cross-sections within the sampling volume, which results in recording of all in-focus particles within that particular plane. Thus, repeating it over multiple cross-sections across the entire sampling volume, enables the detection and segregation of discrete particles within this entire 3-D space. Further details on the holographic imaging technique and its applications can be found elsewhere (e.g., Katz and Sheng, 2010; Talapatra et al., 2013).

The HOLOCAM consists of a 660 nm laser which acts as the coherent illumination source, collimating optics, and a camera recording the holograms at 15 Hz. The entire system is designed to be lowered and raised through the water column, while continuously recording holograms which encapsulate information about the particle fields within the sampling volume. The HOLOCAM was deployed from the boat by

hand, at a slow rate to minimize disturbance while traversing through the water column vertically. This enabled the characterization of particle fields within a size range of  $\sim 1 \mu\text{m}$  to  $\sim 10 \text{ mm}$  in their true state, i.e., without inducing any particle breakage, at least during the downward profiles. It is to be noted that during the upcast, while the system is being retrieved, the sample volume lies in the wake of the system and thus sees well-mixed, turbulent flow which can lead to fragmentation of particles. In fact, prior comparisons of particle size distributions between downcasts and upcasts, have shown a 10–15% decrease in large particle counts ( $> 150 \mu\text{m}$ ) during upcasts, and a corresponding increase in smaller particle populations. Thus, while data was recorded during upcasts, to avoid adding this uncertainty to the data, only the downcasts have been processed for this analysis. At several stations, the system profiled the water column twice in succession, resulting in two downcasts for the relevant station. In such cases, data has been averaged over both downcasts before being presented.

In general, holographic post-processing scheme used here involves three steps: background subtraction, hologram reconstruction, and composite image formation. First, for a given profile, the average image obtained from all the holograms is generated and subsequently subtracted from each hologram. This helps minimize background intensity variations, as well as facilitates removal of static particles, e.g., dust on imaging windows. Second, hologram reconstruction was carried out in  $500 \mu\text{m}$  incremental depth steps over the entire 4 cm sampling volume. Finally, in-focus particles in each reconstructed plane were then consolidated into one composite image. Once the particle list is generated, parameters including area, aspect ratio, major axis length, etc., are used to further isolate both *Microcystis* and *Planktothrix* colonies. Fig. 2 illustrates the entire post-processing methodology as applied to a single

**Table 2**

Data sets.

Source	Chl-a	SPM	PC	HOLOCAM	HPLC	Vertical IOP	AOP	Dates
UNH	20	20	20	13	N/A	14	20	8/19/14–8/21/14
NRL	20	N/A	N/A	N/A	20	11	11	8/18/14–8/28/14

**Table 3**

Details of LIDAR tracks.

Track	Area	Date (mm/dd/yy)	Length (km)	Time (UTC)	Starting lat (degrees)	Starting lon (degrees)	Ending lat (degrees)	Ending lon (degrees)
1	8	8/23/14	8.5	15:55	41.58984	-82.62874	41.51921	-82.66784
2	1	8/19/14	12.1	14:16	41.65756	-82.89373	41.68256	-83.03602
3	1	8/18/14	9.9	14:04	41.69559	-83.21689	41.67456	-83.10139
8	8	8/28/14	7.6	18:28	41.47615	-82.57850	41.54406	-82.58718
10	1	8/17/14	17.2	20:02	41.65555	-83.09680	41.61375	-82.89759
11	1	8/23/14	12.0	14:14	41.75874	-83.08436	41.65276	-83.11452
15	6	8/19/14	4.4	17:49	41.64078	-82.80970	41.60128	-82.80908
16	6	8/19/14	2.5	17:34	41.59858	-82.83004	41.62069	-82.83145
17	6	8/21/14	6.5	15:09	41.60887	-82.74957	41.63797	-82.81722
18	6	8/21/14	0.8	15:21	41.61580	-82.80749	41.61181	82.79889
19	8	8/23/14	5.8	15:49	41.53201	-82.61277	41.56912	-82.66157
21	2	8/24/14	4.5	18:25	41.77124	-83.11100	41.73364	-83.12988
23	2	8/28/14	11.0	20:29	41.79158	-83.22393	41.87998	-83.16398
24	7	8/18/14	19.6	13:39	41.64355	-82.4261	41.64171	-82.66182
26	8	8/21/14	8.3	14:38	41.54451	-82.5388	41.6194	-82.53375
27	7	8/18/14	7.8	13:44	41.64124	-82.72043	41.64541	-82.81355
28	6	8/19/14	5.0	14:15	41.63664	-82.72060	41.64354	-82.77937
30	6	8/19/14	5.2	17:47	41.59639	-82.81330	41.64295	-82.81724
32	4	8/18/14	10.8	20:53	41.80326	-83.31335	41.76710	-83.43442
34	4	8/18/14	11.9	20:21	41.73262	-83.27136	41.69067	-83.40374
35	4	8/18/14	8.8	15:11	41.72162	-83.32837	41.71043	-83.22338
41	5	8/19/14	27.1	17:28	41.83845	-83.05896	41.64809	-82.85441
42	5	8/19/14	11.3	17:22	41.68220	-83.22277	41.76506	-83.14341
44	5	8/21/14	19.3	14:50	41.69493	-82.83242	41.75650	-83.05016
48	9	8/28/14	3.8	19:16	41.47721	-82.73857	41.47657	-82.69286
49	9	8/28/14	2.8	19:11	41.47299	-82.76120	41.47056	-82.79522
50	9	8/28/14	4.0	19:20	41.48353	-82.72931	41.46095	-82.76728

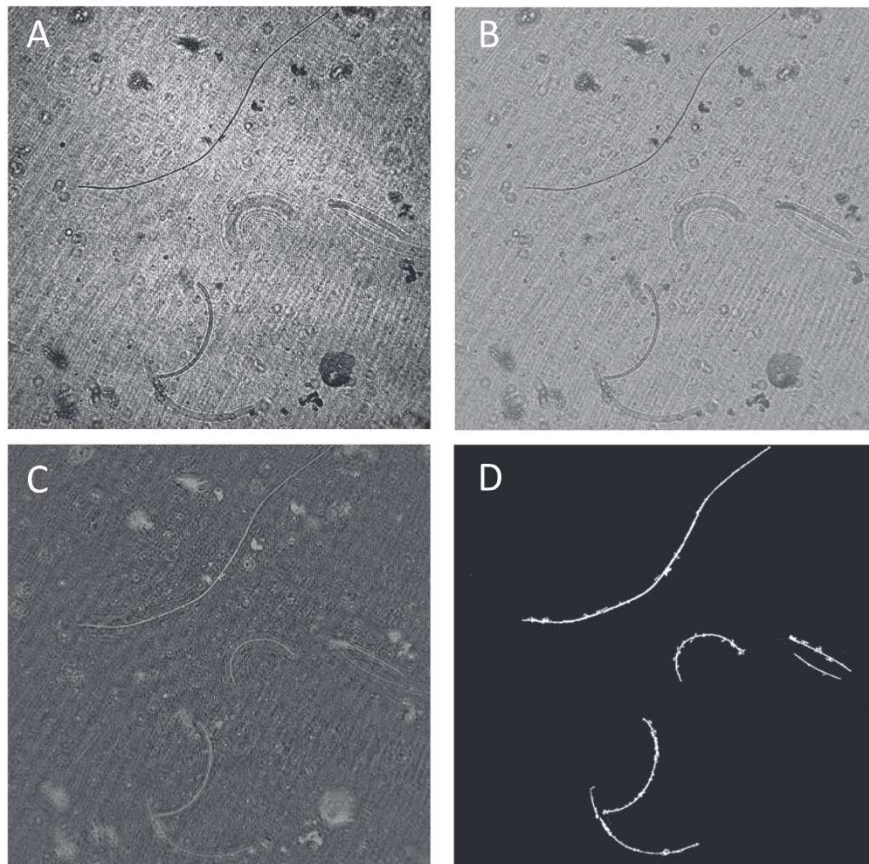


**Fig. 2.** HOLOCAM images from Station S14. A: sample raw hologram with *Planktothrix*; B: background-subtracted hologram; C: post-recon image with all particles in-focus; and D: isolated *Planktothrix* chains after segmentation and thresholding.

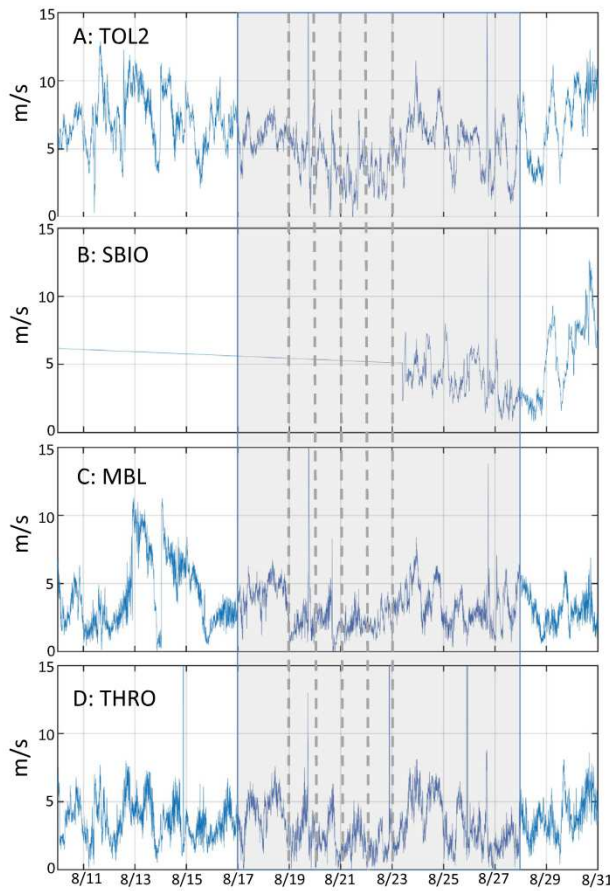


**Fig. 3.** Wind speed measurements from 4 NOAA meteorological stations positioned around the study area (see Fig. 1). A: Toledo Light 2 (TOL2); B: South Bass Island (SBIO); C: Marblehead (MRHO); D: NOS Toledo (THRO). Grey area is period of LIDAR observations; grey vertical dashed lines indicate days with IOP profiles.

hogram containing *Planktothrix* colonies. A more thorough overview of the image processing routines/methodology in creating the particle list from each raw hologram is provided in Nayak et al. (2018). Repeating this procedure for each hologram in a depth profile, provides a vertical distribution of colony number for each species. For *Microcystis*, the empirical relationship of Joung et al. (2006) was used to derive the cell count in each colony based on the surface area. For *Planktothrix* on the other hand, each cell is assumed to be 3.5  $\mu\text{m}$  in length (Churro et al., 2017). Based on this, and knowing the length of the filament of each colony, the number of *Planktothrix* cells were estimated. Cell counts were then binned at 0.5 m depths to generate vertical profiles of cell counts for the two species.

### 2.3.2. Winds

Wind data (speed, direction) were obtained from four different sites with anemometers (Fig. 1) through on-line resources managed and maintained by the National Oceanic and Atmospheric Administration (NOAA). These were Toledo Light 2 (TOL2) - a coast guard tower in western Lake Erie and a part of the Great Lakes Real-time Coastal Observation Network (ReCON), a Coastal-Marine Automated Network (C-MAN) station on South Bass Island (SBIO), a C-MAN station at Marblehead (MRHO) on land near Sandusky Bay, and a C-MAN station near Toledo Harbor (THRO) on land near the mouth of the Maumee River. Raw data points were downloaded and synchronized to the field data collected during the study time period.

### 2.3.3. Remote sensing reflectance measurements

Above-surface  $R_s(\lambda)$  measurements were made with a Field Spec Pro VNIR-NIR1 portable spectrometer system from Analytical Spectral Devices (Boulder, Colorado) for both UNH and NRL data sets. A sequence of radiance measurements of a gray plaque ( $L_g(\lambda)$ ), water surface ( $L_t(\lambda)$ ) and sky ( $L_{sky}(\lambda)$ ) were made and used to derive  $R_s(\lambda)$ . Briefly, the  $L_t$  and  $L_{sky}$  measurements were used to derive an estimate of spectral water-leaving radiance  $L_w$ :

$$L_w(\lambda) = L_t(\lambda) - \rho L_{sky}(\lambda) \quad (3)$$

The reflectance,  $\rho$ , represents the proportion of incident light, which is reflected by a flat water surface at the angle of observation, as determined by Fresnel's equation (Kirk, 1994). The Fresnel reflectance used was 0.028 (Austin, 1972). The downwelling irradiance  $E_d(\lambda)$  was calculated from  $L_g(\lambda)$  assuming that the gray plaque is a Lambertian diffuser as:

$$E_d(\lambda) = \frac{\pi L_g}{R_g} \quad (4)$$

The  $R_g$  derivation from  $L_g$  was based on the spectral reflectivity of the gray plaque (approximately 10% reflection). Above surface  $R_{rs}(\lambda)$  was calculated as the ratio of  $L_w(\lambda)$  to  $E_d(\lambda)$ .

For the NRL measurements,  $R_{rs}(\lambda)$  was computed following the same basic protocol, with some differences in the how surface and sky reflectance were computed. A “white” normalization algorithm was applied over a range of 700 nm to 825 nm rather than the 750 nm specified in Carder and Steward (1985). Further details are provided in the NRL SeaBASS files (Gould, 2014), and in the Ocean Optics Protocols, Vol III, Chapter 3 Method 2 (Mueller et al., 2003).

## 3. Results

During the study period, a cyanobacteria bloom was occurring throughout the southern portion of the western basin extending from Maumee Bay to beyond the islands into the central basin. From a macro point of view, this is considered one bloom, but in fact there was a *Microcystis* bloom occurring in the southern half of the western basin and a *Planktothrix* bloom occurring in the southwest region of the central basin. The northern extent of the Maumee Bay bloom was bounded by the transition zone of the Detroit River plume. The northeastern boundary near the island region was more complex (see Section 3.2). The location of the Detroit River plume front was dynamic, and changed with meteorological conditions. Strong sustained winds were observed from August 12 through August 14 on several of the wind stations (Fig. 3). This altered the hydrography of the western basin, and transported the Detroit River water to the south and encroached into Maumee Bay. Winds decreased from August 17 through August 23, the main window when LIDAR measurements, IOP and holographic profiles were collected. Winds decreased to near or at 0 m/s on August 21 across the entire basin. After August 23, wind speeds increased across the basin.

### 3.1. Horizontal distributions of particles

The surface SPM varied across the region (Fig. 4, Table 4), with highest values in Maumee Bay (Area 4) with a median of 19.4 g/L, and lowest measured values in the Detroit River (Area 3) with a median of 3.3 g/L (Table 4). At sites in the island region (Area 6), the SPM values were intermediate with a median value of 5.1 g/L. The particle fields comprised organic and inorganic types, with the lowest organic content in the Detroit River (Area 3) with a median organic/total ratio of 0.27, and highest in the southeastern western basin (Area 1) with a median of 0.62. The highest ratio was found in this area as well, with a value of 0.79. Inorganic particles were continuously present even in bloom areas, a result of the shallowness of the basin.

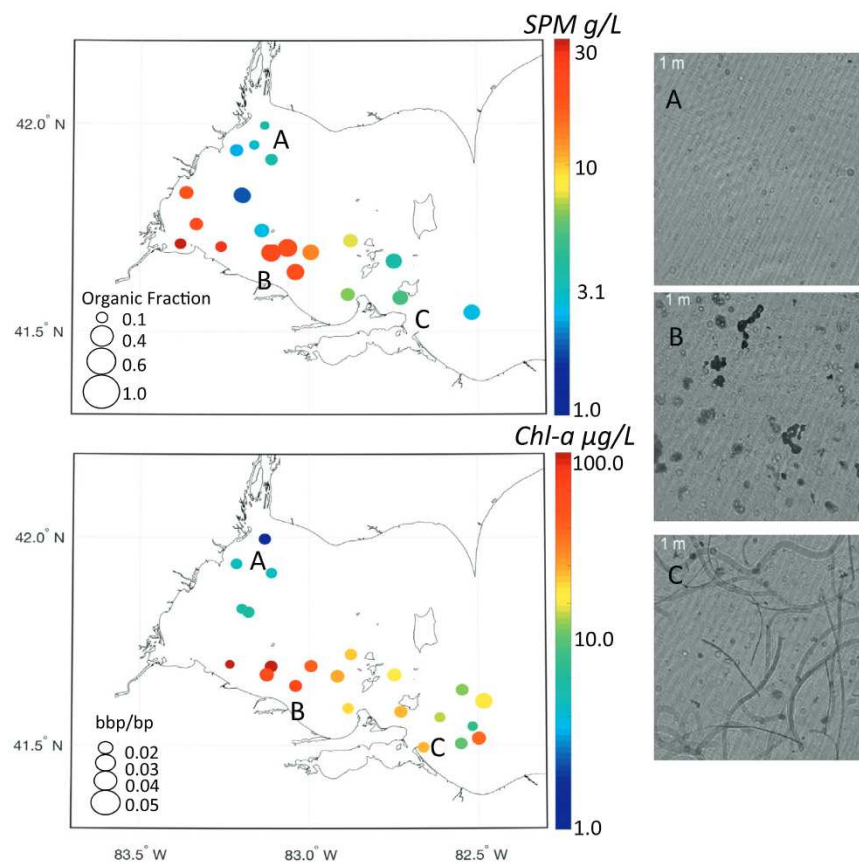


**Fig. 4.** Discrete surface SPM (top left) and *Chl-a* (bottom left) across the study area. Size of circles in top left proportional to organic fraction of SPM; size of circles in bottom left proportional to ratio of particle backscatter to total particle scatter at 443 nm. Right panels show HOLOCAM frame shots from three different areas - A: Area 3 (Detroit River plume); B: Area 1; C: Area 8.

The algal populations were primarily composed of cyanobacteria during the sampling period, although other groups likely co-existed but were not abundant and not recorded. Based on the holographic image data (Fig. 4), we observed *Microcystis* and *Planktothrix* genera present in the western and central basins (Moore et al., 2017). The western basin regions (Areas 1 through 5) were dominated by *Microcystis*, and the central basin regions (Areas 7 through 9) were dominated by *Planktothrix*. The transition region (Areas 6) contained mixtures of the two genera.

### 3.2. Vertical distributions of particles

The vertical particle fields of the different sub-basin areas varied. The driving factors governing the variations in the vertical particle distributions were the wind speed, presence/absence of cyanobacteria and their taxonomic type. The vertical particle patterns were also the driving factor governing the in-water optical properties and associated remote sensing reflectance. These distributions are explored in the following sections in more detail. We present the data organized by sub-region, and examine the coincident measurements where possible.

**Table 4**  
Station biogeochemistry - surface.

Station units	Date	Area	<i>Chl-a</i> µg/L	SPM g/L	PC µg/L	apg490 m <sup>-1</sup>	bbp 490 m <sup>-1</sup>	bbp:bp 490 N/A	Zeaxanthin µg/L	Zea: <i>Chl-a</i> N/A	Kd490 m <sup>-1</sup>
S11	8/20/14	5	22.0	7.4	6.6	0.458	0.132	0.035	N/A	N/A	1.17
S12	8/20/14	6	17.5	3.8	3.3	0.279	0.057	0.044	N/A	N/A	0.59
S13	8/20/14	6	22.7	5.1	3.9	0.371	0.073	0.040	N/A	N/A	0.76
S14	8/20/14	8	7.8	2.7	4.4	0.303	0.043	0.026	N/A	N/A	0.55
S15	8/20/14	6	19.9	6.6	6.8	0.473	0.118	0.029	N/A	N/A	1.09
S17	8/21/14	2	5.8	1.8	3.1	0.201	0.028	0.026	N/A	N/A	0.39
S18	8/21/14	1	41.1	12.6	74.8	0.493	0.223	0.045	N/A	N/A	1.55
S19	8/21/14	1	60.5	18.9	156.9	0.621	0.276	0.039	N/A	N/A	1.91
S20	8/21/14	1	106.3	22.7	213.3	0.500	0.195	0.040	N/A	N/A	1.44
LE3	8/18/14	2	6.1	N/A	N/A	0.251	0.250	0.028	0.301	0.049	0.51
LE4	8/19/14	1	124.3	N/A	N/A	1.024	0.347	0.035	3.248	0.026	2.72
LE5	8/19/14	1	133.8	N/A	N/A	1.301	0.350	0.017	6.203	0.046	3.14
LE7	8/20/14	5	23.9	N/A	N/A	0.490	0.136	0.036	1.223	0.051	1.16
LE8	8/20/14	1	52.9	N/A	N/A	0.909	0.332	0.038	3.135	0.059	2.74
LE9	8/21/14	8	12.1	N/A	N/A	0.413	0.067	0.030	0.922	0.076	0.80
LE10	8/21/14	8	22.7	N/A	N/A	1.349	0.088	0.023	1.550	0.068	2.17
LE11	8/22/14	8	38.5	N/A	N/A	0.708	0.060	0.038	2.904	0.076	1.11
LE12	8/22/14	8	16.0	N/A	N/A	0.941	0.097	0.053	1.434	0.090	1.83
LE14	8/23/14	8	10.2	N/A	N/A	0.422	0.049	0.029	0.776	0.076	0.82
LE15	8/23/14	8	13.7	N/A	N/A	0.528	0.054	0.021	1.086	0.080	1.01

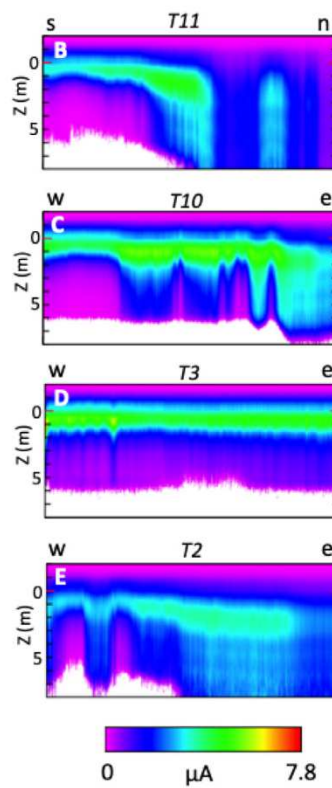
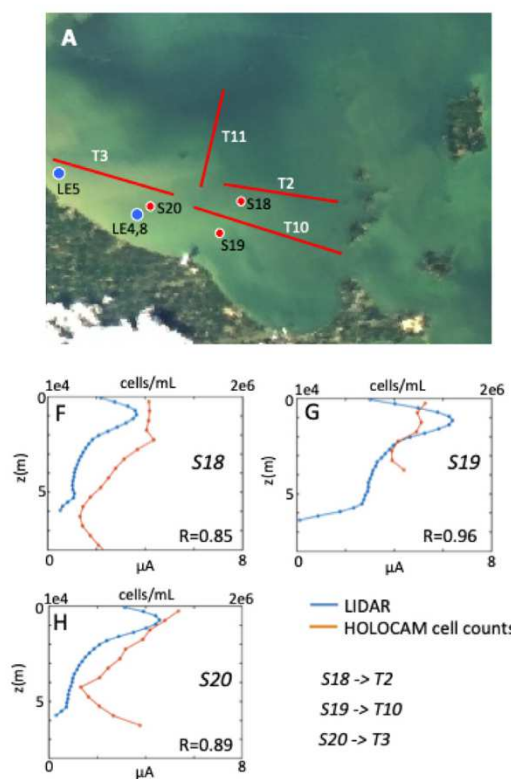


**Fig. 5.** Echograms from LIDAR tracks and matched holographic profiles in Area 1. A: RGB image from Landsat-8 showing selected LIDAR transect lines and stations S18, S19 and S20 (sampled on August 21); B: Track T11 from August 23, 2014; C: Track T10 from August 17, 2014; D: Track T3 from August 18, 2014; E: Track T2 from August 19, 2014; Note: y-axis for all echograms extends from 8 m depth to 2 m above the surface; x-axis for all echograms are relative along-track distances scaled to actual distances contained in Table 3. From left to right, track orientations are south to north (Track T11) or west to east (Tracks T10, T3 and T2). Color scale has a range of 0–7.8 A m<sup>2</sup> proportional to particle concentration; F–H: cell count totals of *Planktothrix* and *Microcystis* versus depth (red), along with the depth profile of LIDAR return signal strength (blue) from nearest track and location for stations S18, S19 and S20. Note: horizontal scales for cell counts (top of plot) and LIDAR (bottom of plot) are on absolute scales for comparison. Further track details contained in Table 3. (For interpretation of the references to color in this figure legend, the reader is referred to the web version of this article.)

### 3.2.1. Area 1: the southeastern region of the western basin

The highest concentrations of algal particles and *Chl-a* were found in this region during the study period. This area was sampled directly on August 20 and 21, 2014, and was observed by the aircraft LIDAR on three consecutive days from August 17 through August 19, 2014 (Fig. 5). In all tracks, particles were concentrated towards the surface in a layer one to 2 m thick - a ubiquitous feature from this area. The surface features also followed bathymetric features in some but not all echograms. These similarities exist in other transect data from other areas (e.g., Area 2). We believe the surface features result from particles and not artifacts of the processing. These are interesting features nonetheless, but we do not explore this subject further.

The surface features were prominent over a number of days when winds were 5 m/s or less. Particle fields in tracks T11 and T2 also showed surface layers losing form and diminishing in northward directions on the edges of the cyanobacteria bloom to non-bloom waters. Particles in these transitions appear to dilute and spread vertically from the surface layer towards the bottom, and a similar pattern was present in the eastern end of track T10 (near the transition into the central basin).

In this area, holographic image analysis showed a large portion of the particle field was dominated by cyanobacteria, specifically *Microcystis*. We compared the LIDAR vertical patterns to overall cyanobacteria cell counts from holographic station profiles from matchups. The LIDAR tracks and the station profiles were not exactly coincident in space and time. Although stations were generally within several km to the nearest track location (Table 5), the temporal difference was several days. This is not ideal, as these differences introduce mismatch errors into the comparisons. However, the surface layer feature in this area was a persistent feature over the course of days. The correlations between cyanobacteria cell counts and the LIDAR return signal strength were high for the stations this area, ranging from 0.85 to 0.96 (Fig. 5F–H). The LIDAR patterns were a good descriptor for the cyanobacteria distributions here.

Examining the distributions of the two main genera, *Microcystis* cell

**Table 5**  
LIDAR - discrete station matchups.

Station	Track ID	Nearest track lat units	Nearest track lon (degrees)	Distance (km)	Time difference (days)	R
S11	T41	41.694	–82.904	3.6	1.3	–0.13
S11	T44	41.707	–82.881	1.4	1.0	0.30
S12	T27	41.641	–82.748	3.1	2.0	0.78
S13	T19	41.577	–82.669	5.0	3.0	0.45
S14	T26	41.547	–82.537	1.7	0.9	0.64
S17	T23	41.827	–83.197	0.1	7.3	0.06
S18	T2	41.673	–83.003	2.0	2.0	0.85
S19	T10	41.644	–83.039	0.1	3.8	0.96
S20	T3	41.675	–83.114	2.0	3.1	0.89
Average				1.86	2.7	0.53

concentrations were highest near the surface at the three stations (S18, S19 and S20) with levels exceeding  $1 \times 10^6$  cells mL<sup>–1</sup> (Fig. 6A). *Planktothrix* cells were also observed, but were lower in number (less than  $2 \times 10^4$  cells mL<sup>–1</sup>) and followed different vertical profile structures (Fig. 6B). None of these three stations showed a surface maxima for *Planktothrix*. Stations S19 and S20 showed sub-surface maxima at 2 m and 4 m deep, respectively, below the maxima of the *Microcystis*, while S18 showed a more uniform distribution. Vertically-normalized cell count ratios (by integrated column sum) of *Microcystis* to *Planktothrix* showed a decrease from the surface to a depth of about 4 m, then increased towards the bottom at all stations (Fig. 6C). There was an uneven vertical distribution of these two populations, with *Planktothrix* increasing over *Microcystis* through depth. The increase in *Microcystis* cells at the bottom was likely from *Microcystis* cells/colonies having sunk.

Water temperature profiles indicate some thermal variation with warmest waters near the surface (Fig. 6D). This enhanced stratification would favor *Microcystis* surface accumulation/retention. Surface  $b_{hp}$  at 443 nm (in Area 1) ranged over a factor of two ( $0.2 \text{ m}^{-1}$  to  $0.4 \text{ m}^{-1}$ ),

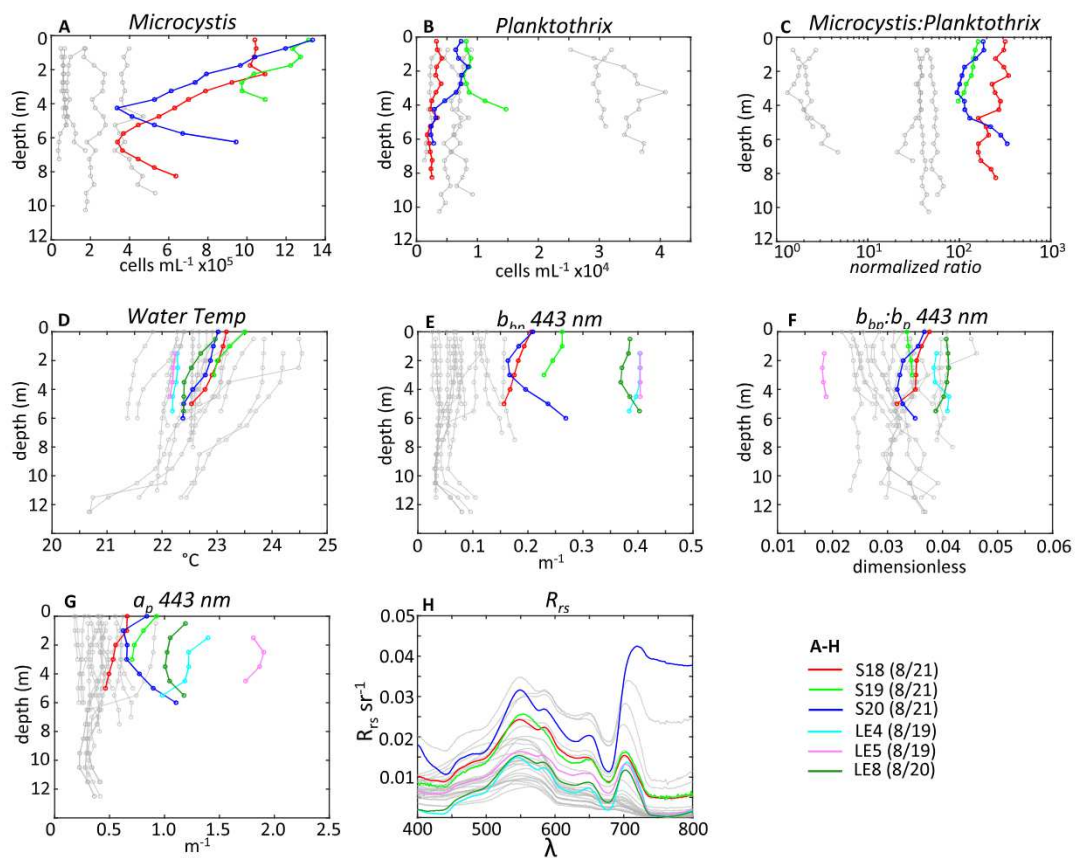


**Fig. 6.** Holographic and IOP vertical profile data are highlighted for stations S18, S19 and S20 in Area 1 sampled on Aug. 21, 2014, and IOP-only profiles for stations LE4, LE5 (sampled on Aug. 19, 2014) and LE8 (sampled on Aug. 20, 2014). A: *Microcystis* counts; B: *Planktothrix* counts; C: cell count ratio normalized to column integrated sum for *Planktothrix* and *Microcystis*; D: water temperature; E: particle backscatter at 443 nm; F: particle backscatter ratio at 443 nm; G: particle absorption at 443 nm; H: above-water  $R_{rs}$ . Note: grey lines in plots A through H indicate profiles of all other stations not in the area for comparative visualization.

and station LE5 was oversaturated, as evident in the  $b_{bp}$  profile (Fig. 6E). Omitting this station, this area had the highest  $b_{bp}$  values recorded during the study period. There were also variations in the profile structure, with S20 showing a strong vertical gradient. High values were found at the surface and towards the bottom. High  $b_{bp}$  ( $> 0.03$ ) and particle absorption coefficients indicate the dominance of gas-vacuolate cyanobacteria on the backscattering efficiency (Fig. 6F, G).

The  $R_{rs}$  spectra from this area contain features in the red/NIR (Fig. 6H), also consistent with high biomass - a trough at 675 nm and high peaks at 555 nm and 709 nm. The high features in  $R_{rs}$  beyond 700 nm from S20 optically resemble land vegetation (Hu et al., 2010; Kutser, 2004). Although the particle fields in Area 1 are part of the same broader population, the  $R_{rs}$  NIR signal from S18 and S19 are well below that of S20, and highlights a difference in  $R_{rs}$  between populations just below the water interface and at the surface (Kutser, 2004).

### 3.2.2. Areas 2, 3 and 5: northern transition edges in the western basin

The Detroit River plume (Area 3) was sampled in the field and by the aircraft on the same day on August 19, 2014. There were few particles (and virtually no cyanobacteria) in the water relative to other areas, and contained few noteworthy features in the vertical structure (not shown). The more interesting particle features were the transitions from cyanobacteria to non-cyanobacteria waters, located between the southern and northern half of the western basin. Echograms from tracks in Areas 2 and 5 highlight these transitions (Fig. 7). These tracks were flown on different days (Table 3), and likely reflect some changes in water structure from winds. Particles were concentrated near the surface and sharply discontinuing at transitions into waters associated with the Detroit River plume in the western half of tracks T41 and T44, and

northern part of track T42. Track T44 was flown a few days after track T41, during a period when winds were decreasing to minimal levels on August 21 when track T44 was flown.

A station was sampled towards the eastern segments of these tracks (station S11) with the HOLOCAM. The cell counts and LIDAR strength of the nearest track point on T44 have a low correlation ( $R = 0.30$ ) (Fig. 7G). Winds were strong enough (5 to 10 knots) from August 19 to August 20 when track T41 and station S11 were observed to prevent the surface layers of cyanobacteria forming in this area, which were low in overall concentration relative to Area 1 stations. Track T41, parallel to track T44, was flown on August 19, a day before the station profile. The nearest LIDAR profile from this track to station S11 shows a lower particle maximum than track T44, and it appears the whole profile is offset by a meter or so. The features in this profile are also slightly offset from features in the holographic profile, leading to a negative correlation ( $R = -0.13$ ). From these three profiles, taken on consecutive days, it appears that the particle field was moving upward as winds were decreasing, resulting in a weak near-surface layer to form on August 21.

Tracks T21 and T23 were flown days later after wind increases across the basin between August 23 and August 25 (Fig. 3). Particles were more dispersed throughout the water column and a more gradual northward transition occurred on track T21 compared to track T42. Particle distributions from along track T23 (August 28) showed a transition between north and south, with a high number of particles distributed through the water column in the southern half. The southern portions of these tracks are connected to the particle fields from Area 1 and belong to the same cyanobacteria bloom. Station S17 was sampled near track T23. The correlation between holographic cell counts and the nearest LIDAR track point was poor ( $R = 0.06$ )

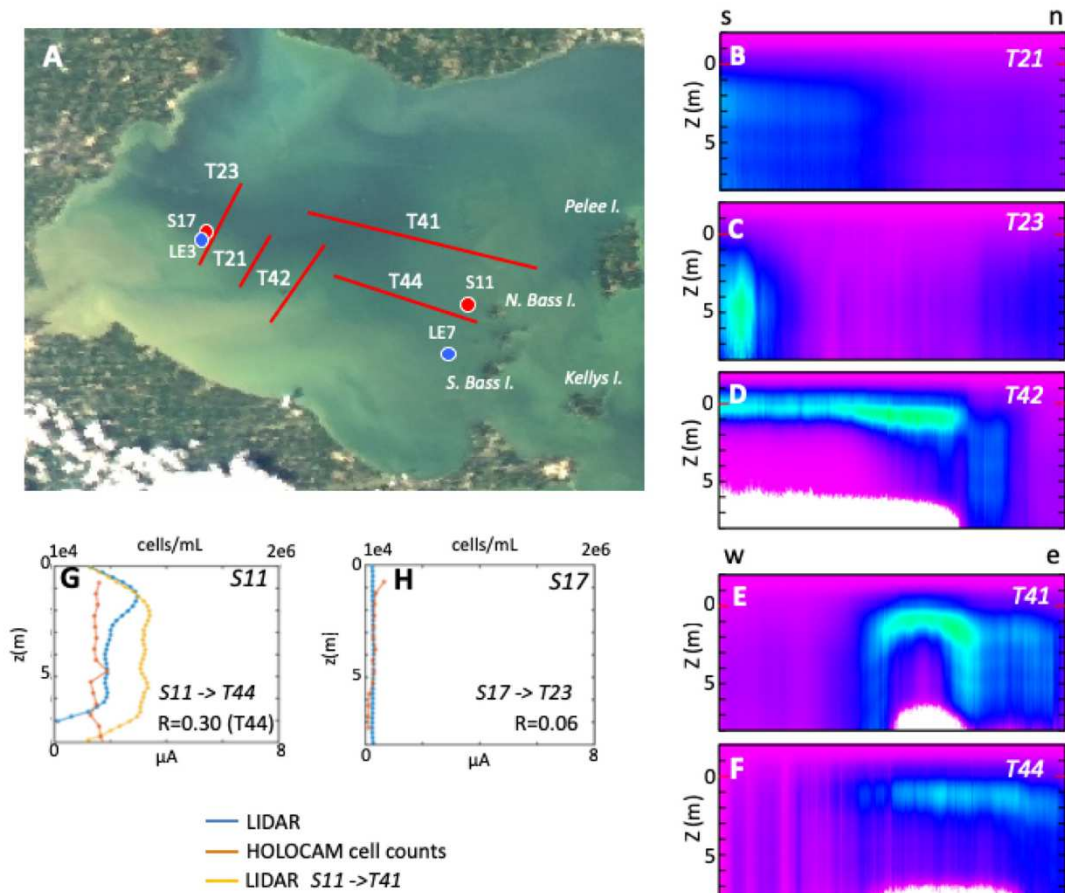


**Fig. 7.** Echograms from Areas 2 and 5 flown across particle heavy southern areas to particle-free northern areas of western basin. A: RGB image from MODIS-Aqua showing selected LIDAR transect lines and station locations; B–D: Tracks T21, T23 and T42 in a south to north orientation (left to right); E and F: Tracks T41 and T44 in a west to east orientation (left to right); G and H: cell count totals of *Planktothrix* and *Microcystis* versus depth (red), along with the depth profile of LIDAR return signal strength (blue) from nearest track and location for stations S11 and S17, respectively. Station S11 was also matched to a second track - T44 (yellow line). Note: horizontal scales for cell counts (top of plot) and LIDAR (bottom of plot) are on absolute scales for comparison; echogram color scale same as Fig. 5. Further track details contained in Table 3. (For interpretation of the references to color in this figure legend, the reader is referred to the web version of this article.)

(Fig. 7H). In this case, the time difference was over 7 days, and not expected to be highly correlated, although both LIDAR and cell counts were low relative to other stations.

Four profiles of IOPs (two paired with HOLOCAM profiles) were made in this area. Cyanobacteria counts for both *Microcystis* and *Planktothrix* were low relative to Area 1 (where the bloom was most intense), particularly Station S17 which was between the bloom area and the Detroit River plume front (Fig. 8A–C). The vertical profiles of the cyanobacteria counts showed less structure and were more uniform compared to the profiles from Area 1, but normalized cell ratios decreased for *Microcystis* relative to *Planktothrix* at station S17.

Profiles of water temperature showed a mostly uniform structure at all stations, and the IOP profiles also were uniform vertically (Fig. 8D). The  $b_{bp}$  values ranged from  $0.02 \text{ m}^{-1}$  to  $0.15 \text{ m}^{-1}$  throughout the water column, much lower than those from Area 1 (Fig. 8E). In comparison, station S11 contained higher cyanobacteria counts,  $\tilde{b}_{bp}$  and  $R_{rs}$ . Optically and ecologically, this station was still in the bloom region. Station LE7 (no HOLOCAM data), near Station S11, also had high  $b_{bp}$  in the IOP profile (Fig. 8F) and similar  $R_{rs}$  shape but lower magnitude than S11 (Fig. 8H). For S17 and LE3,  $R_{rs}$  were much lower with no spectral features in the red/NIR, and are considered as outside the bloom.

### 3.2.3. Area 6: transition zones in the island region

In contrast to Area 1, the particle distributions were more dispersed from about 2 m depth down to 8 m approaching the bottom in the island region (Fig. 9). There were no distinct surface layers present in the

echograms. There was horizontal variability along some tracks, notable track T15 and T16 with particles appearing more concentrated in the northern ends. Tracks T17 and T18 were taken in the same region but a few days after tracks T15 and T16, and show weaker particle concentration yet the same dispersed pattern from the surface down to 8 m. The echogram for track T27, an east-west track linking the island region to the central basin, shows moderately high particle concentrations distributed throughout the water column, with a slight sub-surface maximum forming at the western edge of the track closer to the islands. The hologram profile near this track showed low cell counts overall, and good agreement with the LIDAR data ( $R = 0.78$ ) (Fig. 9H). Further in the south below Kellys Island, a diffuse particle distribution was detected with higher concentrations away from the surface. A nearby station with holographic data also showed a weak, diffuse cell count profile (station S13) and the correlation is weaker ( $R = 0.45$ ), but both LIDAR strength and cell count totals were low. The time difference (three days) may explain the low correlation for this pairing.

We found mixtures of *Microcystis* and *Planktothrix* at stations within and around the islands (Fig. 10A–C). Relative to stations from other areas, there were high amounts of *Planktothrix* at station S12 ( $3 \times 10^4 \text{ cells mL}^{-1}$ ) in the middle of the island formation, with a mostly uniform vertical profile and a weak increase towards the surface. Very few *Microcystis* colonies were observed here (less than  $2 \times 10^5 \text{ cells mL}^{-1}$ ). We note that *Microcystis* cells/colonies were difficult to visually identify from other particles in the image processing of the HOLOCAM data. These particles were low in concentration

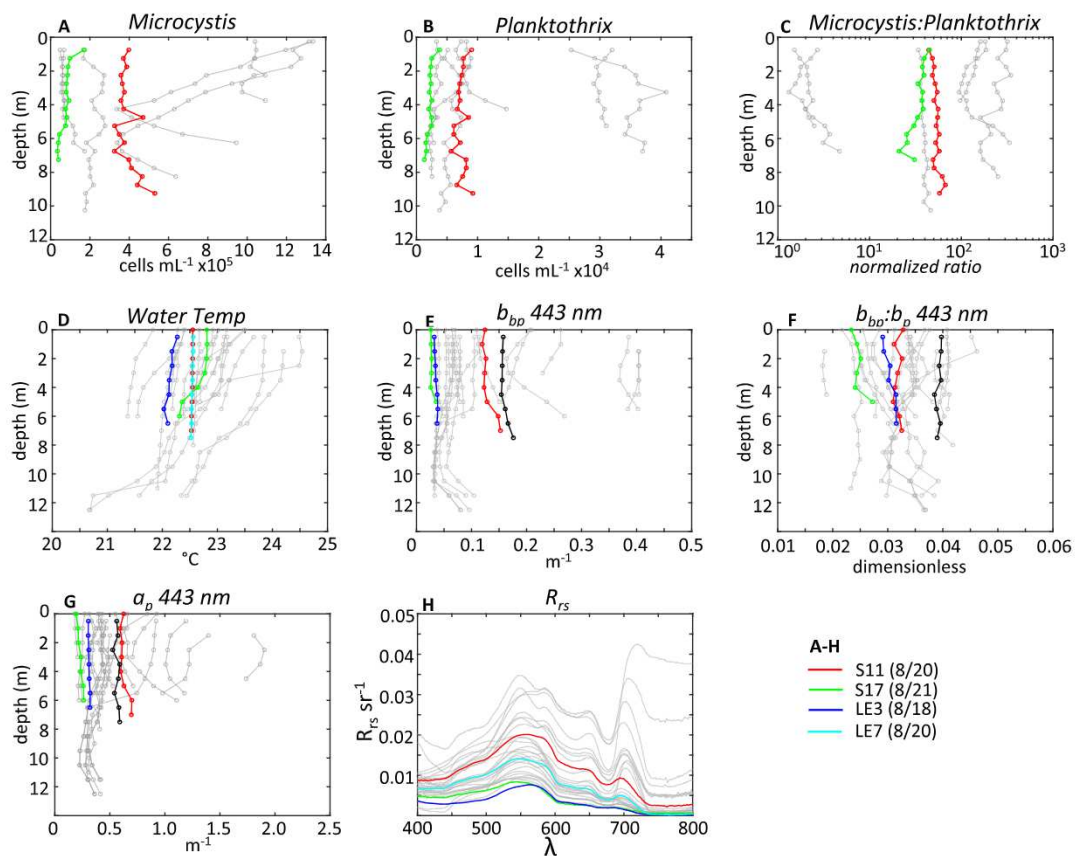


**Fig. 8.** Holographic and IOP vertical profile data for stations S11 and S17 are highlighted. IOP-only profiles for LE3 and LE7 are included. A: *Microcystis* counts; B: *Planktothrix* counts; C: cell count ratio normalized to column integrated sum for *Planktothrix* and *Microcystis*; D: water temperature; E: particle backscatter at 443 nm; F: particle backscatter ratio at 443 nm; G: particle absorption at 443 nm; H: above-water  $R_{rs}$ . Note: gray lines in plots A through H indicate profiles of all other stations not in the area for comparative visualization.

throughout the water column, but were counted as *Microcystis* and may be an overestimate. The other two stations with holographic data (S13 and S15) - both at the southern end of the island channel connecting the central and western basins - had similar vertical profiles for *Planktothrix*. Both stations contained high cell counts (greater than  $3 \times 10^4$  cells  $\text{mL}^{-1}$ ) with non-uniform vertical distributions concentrated at depths of about 3 m. These sub-surface maxima were about twice as high as the surface concentrations, and remained high from this maxima layer to the bottom at 7 m. Station S12 had a uniform temperature structure, but stations S13 and S15 showed a surface warming with potential gradients setting up. Sub-surface *Planktothrix* maxima are below this, while in Area 1 *Microcystis* maxima were in the warming surface layer (Fig. 10D).

Optical properties increased weakly over depth for  $b_{bp}$ ,  $\tilde{b}_{bp}$  and  $a_p$  (Fig. 10E–G), consistent with holographic cell counts. The  $R_{rs}$  spectra for all three stations exhibit a broad peak at 550 nm with weaker but identifiable red/NIR features, indicative of moderate particle concentrations in the surface (Fig. 10H). The “U” shape between 670 nm and 709 nm however is evident but the depression at 620 nm (from phycocyanin absorption) is not pronounced.

#### 3.2.4. Area 8: southeast of islands

This area contained the most discrete stations and is well represented by IOP profiles and LIDAR tracks. However, only one station (S14) contained a HOLOCAM profile. The echograms from this area contain varying patterns, but all show dispersed particles evenly distributed through the water column and no surface accumulation. Particle concentrations were low in the water column in tracks T1, T19 and T26 (Fig. 11). These tracks are all outside Sandusky Bay to the northeast of the mouth. Conversely, moderate particle concentrations

were disbursed evenly, with a slight indication of sub-surface maxima several meters below the surface (2 to 3 m depth) in tracks T8, T27 and T28 (in the middle of the islands in Area 6). Particle concentrations were elevated throughout the water column on the northern end of track T30 near Area 1, and were lowest overall in the eastern segment of track T24. An elevated sub-surface particle field extending from 3 m to 10 m with even distribution is seen towards the western end of the segment. This pattern continues for the remainder of track T24 with an abrupt increase in particle concentration near the western edge. This track continued into track T27 (see Section 3.2.3).

The lone holographic profile (station S14) was matched to LIDAR track T26 (Fig. 11H). The cell counts for this station were lower relative to stations from other areas, although not the lowest. The vertical structures of cell counts and LIDAR signal strength follow the same pattern - lower at the surface with a deeper, relatively constant level, and showed a moderate correlation ( $R = 0.65$ ), with a time difference of less than a day. The vertical patterns for both *Microcystis* and *Planktothrix* were similar (Fig. 12A–C). There was a cell maximum was below the surface at around 3 m depth accompanied with weak, featureless changes in normalized cell ratios. Water temperature profiles had more vertical variation than other areas, and most stations exhibited warmer temperatures at the surface (Fig. 12D). Station LE12, located at the northern end of track T26, showed the strongest thermal gradient with stratification setting in the top 2–3 m. The other stations displayed more gradual changes.

Surface  $b_{bp}$  were low overall relative to Area 1, and showed weak vertical structure except station LE12 where a shallow thermocline developed (Fig. 12E). Some profiles also contained bottom increase, which could be re-suspended sediments or colonies that have sunk. The  $\tilde{b}_{bp}$  varied over a wide range at the surface (Fig. 12F), with highest

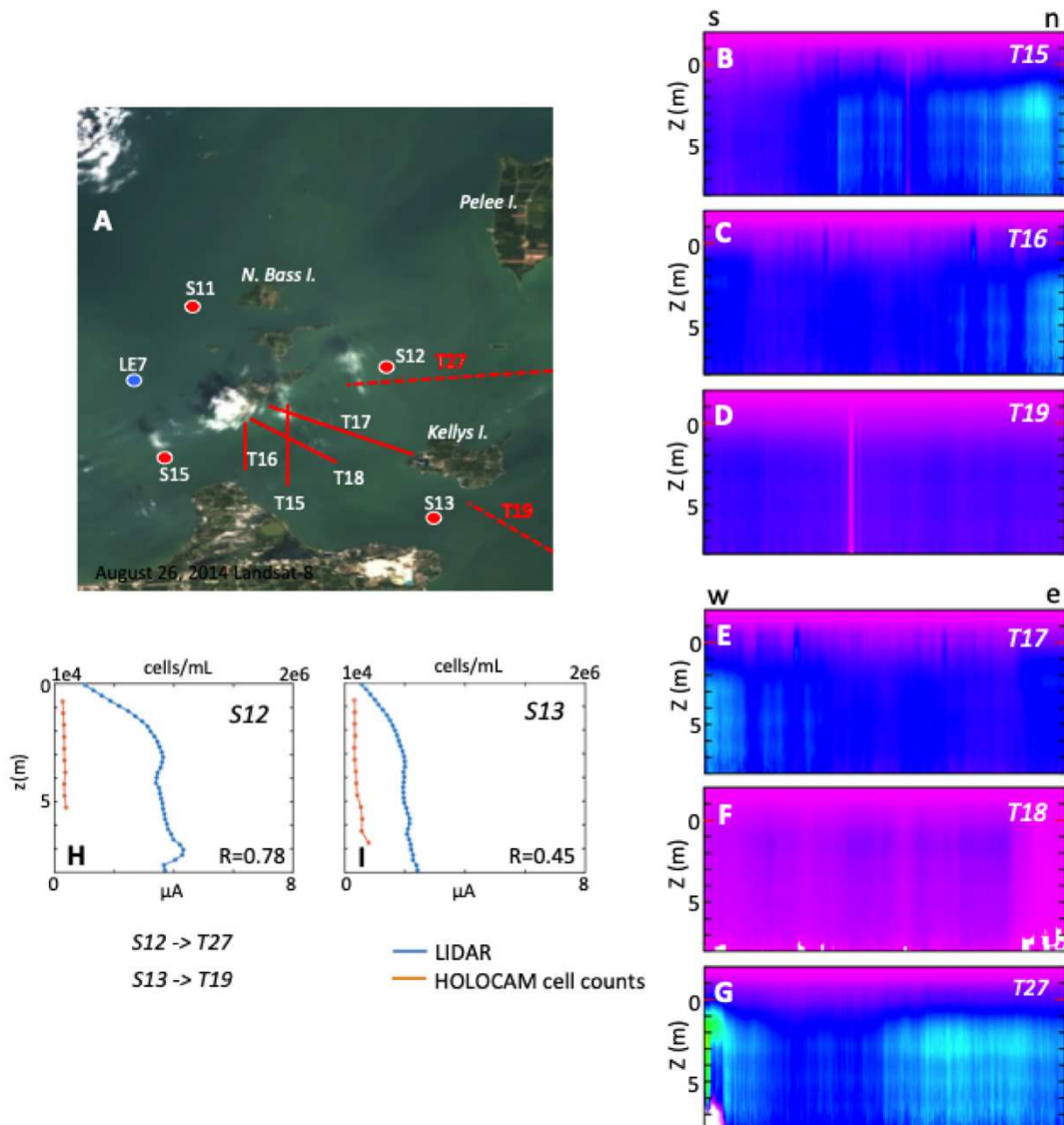


**Fig. 9.** Echograms from tracks in Area 6. A: RGB image from MODIS-Aqua with selected LIDAR transect lines; B–D: Tracks T15, T16 and T19 in a south to north orientation (left to right); E–G: Tracks T17, T18 and T27 in a west to east orientation (left to right); H and I: cell count totals of *Plantkothrix* and *Microcystis* versus depth (red), along with the depth profile of LIDAR return signal strength (blue) from nearest track and location for stations S12 and S13. Note: horizontal scales for cell counts (top of plot) and LIDAR (bottom of plot) are on absolute scales for comparison; echogram color scale same as Fig. 5; dashed lines indicate tracks continuing off map. Further track details contained in Table 3. (For interpretation of the references to color in this figure legend, the reader is referred to the web version of this article.)

value at station LE12 (along with stations LE9 and LE14), which is an indication of dominance by gas-vacuolate cyanobacteria. Stations with lower values (S14, LE10 and LE15) may have contained cyanobacteria, but the particle fields may not have been dominated by them. Vertical structures of  $b_{bp}$  at stations LE11 and LE12 showed near-surface maxima, while the profiles at stations LE10 and LE15 showed increasing values with depth. Values are above 0.03 starting at depths below 6 m, indicating a deeper cyanobacteria population. The  $a_p$  values were high at the surface in some stations, and also at the bottom (LE11 and LE12) which also indicate a bottom population (Fig. 12G).

The  $R_{rs}$  spectra all contained a peak at 550 nm (Fig. 12H), as well as red/NIR features associated with cyanobacteria - shoulder peaks at 650 and 709 nm forming the “U” shape. These features are weaker and less prominent compared to  $R_{rs}$  from other areas. Notable among this group, station LE12 containing the highest  $R_{rs}$  magnitude and deep spectral features in the red/NIR. This was an unusual station that stands out from the other stations in this area, and the pronounced surface thermal layer that may have acted to maintain cyanobacteria cells near the

surface, consistent with this station's  $R_{rs}$  spectra and IOP profiles.

### 3.3. Light levels and cell distributions

The spatial distribution of light attenuation at 490 nm ( $K_d490$ ) was examined for connections with vertical population structure (Fig. 13A). The derived  $K_d490$  varied across the region geographically, and the mean value for the southern half of the western basin ( $= 2.17 \text{ m}^{-1}$ ) was double that of the central basin (mean of  $1.02 \text{ m}^{-1}$ ). The algal communities themselves modified  $K_d490$  through cellular absorption and scattering processes, and was more pronounced in the surface waters in the western basin (Area 1). The  $K_d490$  patterns explain differences in sub-surface maxima of the *Planktothrix* communities between areas. In the western basin (Area 1), *Planktothrix* maxima were closer to the surface where light was attenuated more rapidly compared to the areas in the island region and central basin.

Zeaxanthin, a photoprotective pigment found in both *Microcystis* and *Planktothrix* (Desey et al., 2009; Schagerl and Müller, 2006), and

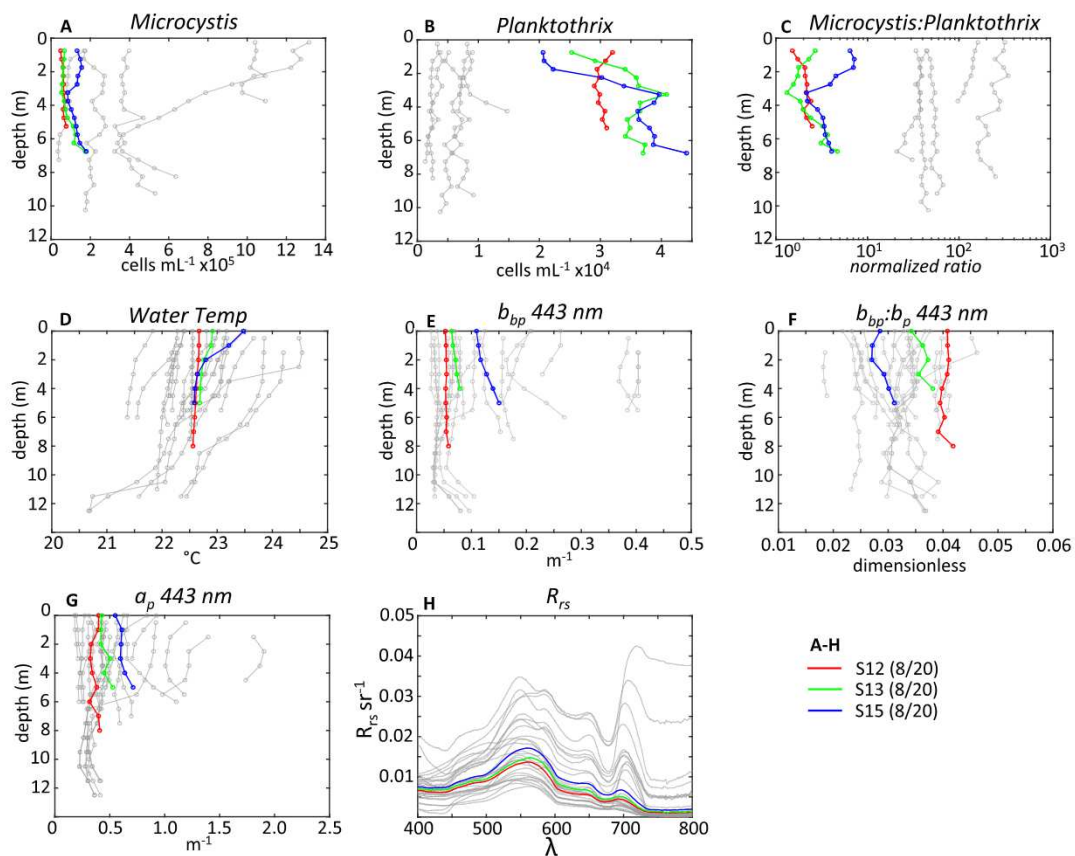


**Fig. 10.** Holographic and IOP vertical profile data are highlighted for stations S12, S13 and S15 in the island area (Area 6) sampled on August 20, 2014. A: *Microcystis* counts; B: *Planktothrix* counts; C: cell count ratio normalized to column integrated sum for *Planktothrix* and *Microcystis*; D: water temperature; E: particle backscatter at 443 nm; F: particle backscatter ratio at 443 nm; G: particle absorption at 443 nm; H: above-water  $R_{rs}$ . Note: gray lines in plots A through H indicate profiles of all other stations not in the area for comparative visualization.

the ratio of zeaxanthin to total *Chl-a* (*zea/Chl-a*) in surface waters were also mapped (Fig. 13B). The highest concentrations of zeaxanthin occurred in the western basin, but the higher *zea/Chl-a* occurred in the island and central basin region (mean of 0.080), and lower *zea/Chl-a* (mean of 0.054) were measured in the western basin. *Planktothrix* has been reported to have a higher *zea/Chl-a* than *Microcystis* in laboratory culture at similar light levels (Schlüter et al., 2006), suggesting that *Planktothrix* cells required more photoprotection from light.

From  $K_d490$ , the optical depth ( $Z_{10}$ ) was derived (Eq. (2)), yielding the depth where 10% of the light remains. The depths of the *Planktothrix* cell maxima were derived from the HOLOCAM profiles (Fig. 13C). Deeper *Planktothrix* maxima were observed in clear waters (higher  $Z_{10}$ ). From this, we believe that low winds, light intensity and water clarity were prime determining factors in influencing the vertical *Planktothrix* distributions across the region.

The surface concentrations of all cyanobacteria cells were an order of magnitude less than the water column total when integrated over the full depth range from the holographic dataset. There was a consistent log-linear relationship between surface cell concentration and total column counts for both genera, combining to form a continuum (Fig. 13D). The lower cell concentration range ( $< 10^5$ ) is occupied by *Planktothrix*, and the higher range is occupied by *Microcystis*. The highest cell counts for *Planktothrix* were below the lowest cell counts for *Microcystis*. The mean ratio of *Microcystis* surface cells to column integrated cells was 0.22, whereas the mean ratio for *Planktothrix* was 0.13. On a relative basis, *Microcystis* cells were nearly two times the concentration of *Planktothrix* cells, a majority of which were dispersed throughout the water column.

Penetration depths of the LIDAR were greater than the optical depths reported above. For the Detroit River plume (not shown), LIDAR

penetration depths ranged from 12.4 m to 13.2 m. Around the islands, we saw values from 10.7 m (track T1) to 12.3 m (track T26). Penetration depths in the western basin ranged from 5.5 m (track T3) to 8.2 m (track T2), with even lower values in Maumee Bay (4.4 m, track T34). These depths are deep enough to reach the bottom in most places in the western basin. Penetration depths were highest in the central basin (17.4 m, track T5), but often did not reach the bottom. The effect of limited penetration depth is that cyanobacteria below that depth will not be measured by the LIDAR. For example, *Microcystis* cell counts increased at depths below about 6 m at station S18. This increase was not seen in the nearby LIDAR profiles, which had penetration depths of about 5.5 m.

The LIDAR penetration depth and the optical depth are related, but both describe different aspects of light transmission/attenuation in the water column. The optical depth was derived from surface values for the IOPs using a marine model and predicts the depth where 10% of the light remains assuming homogenous water and does not account for variations within the water column, whereas the LIDAR penetration depth was based on the detection of return of photons throughout the water column. Despite these and time/space differences already mentioned, there is a positive correlation between the LIDAR penetration depth and  $Z_{10}$  based on the discrete stations and the LIDAR tracks ( $R = 0.93$ ) (Fig. 14). A non-linear relationship is evident between the two variables, but this is expected, as the light decay is exponential and the IOP vertical structures are heterogeneous in many locations. Based on this comparison, we believe the LIDAR resolves the particle structure at greater depths than expected when just considering  $Z_{10}$  depths.

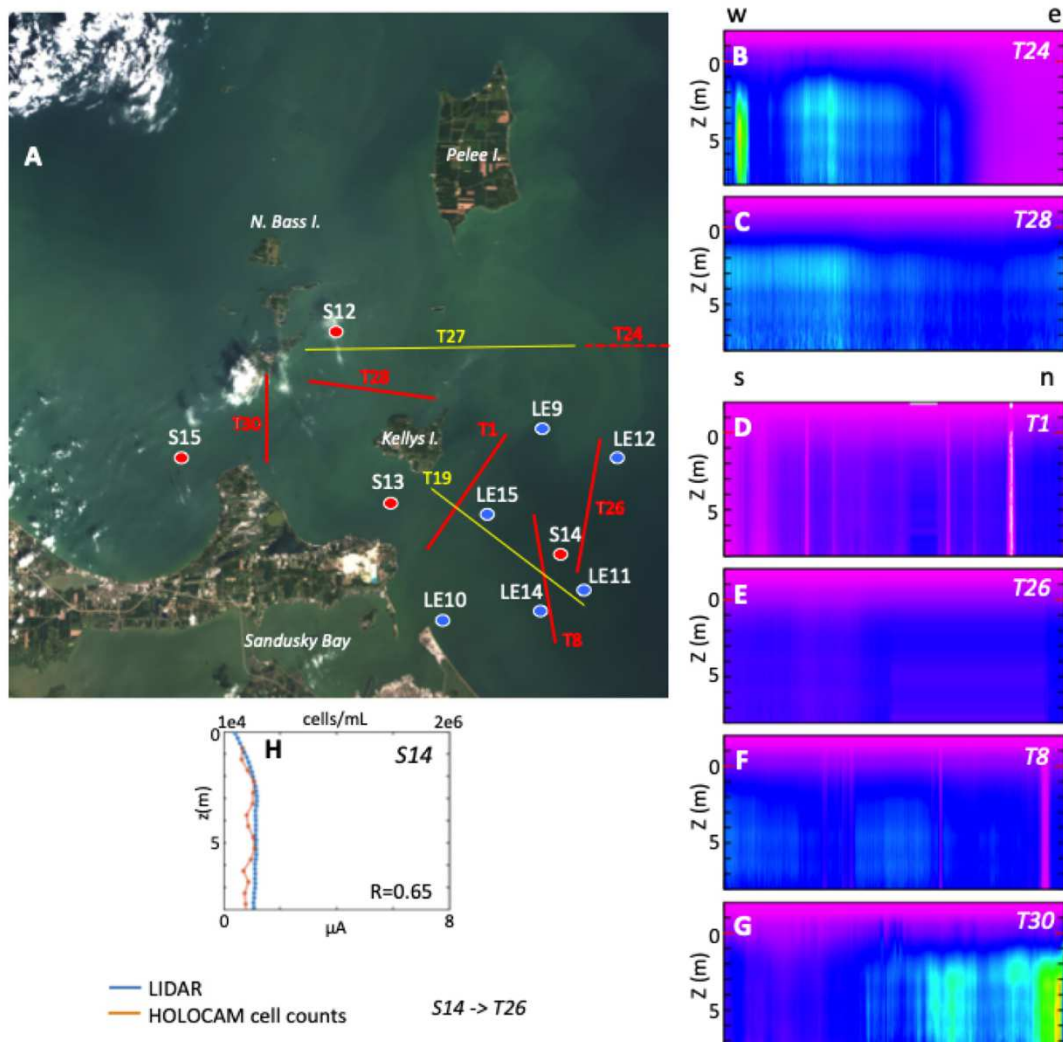


**Fig. 11.** Echograms from tracks in Area 8. A: RGB image from Landsat-8 with selected LIDAR transect lines; B and C: Tracks T24 and T28 in a west to east orientation (left to right); D–G: Tracks T1, T26, T8 and T30 in a south to north orientation (left to right); H: cell count totals of *Planktothrix* and *Microcystis* versus depth (red), along with the depth profile of LIDAR return signal strength (blue) from nearest track and location for station S14. Note: horizontal scales for cell counts (top of plot) and LIDAR (bottom of plot) are on absolute scales for comparison; echogram color scale same as Fig. 5; yellow: echograms for these tracks are contained in Fig. 9; dashed lines indicate tracks continuing off map. Further track details contained in Table 3. (For interpretation of the references to color in this figure legend, the reader is referred to the web version of this article.)

#### 4. Discussion

##### 4.1. Vertical distributions of particles using LIDAR and holography

A main objective of the study was to use a combination of LIDAR and cell counts from holography to describe the three-dimensional distribution of a cyanobacteria bloom in Lake Erie. The LIDAR observations and the profile structure of cell counts largely agree, despite the differences in time and space between the nearest stations and LIDAR track. These measurements were not planned to be coincident, as they were from individual projects that were not coordinated. Nonetheless, there was good opportunity to compare the two data sets, as the number of LIDAR tracks was extensive over the study region. The correlation between cyanobacteria cell counts and the LIDAR signal strength ranged from  $-0.13$  to  $0.96$  with an average of  $0.53$ . These were surprisingly high given the differences in time and space. We also note that the LIDAR signal is a function of all particles in the water, and we only quantified the cyanobacteria cell counts for two genera which were dominant.

We believe that most of the LIDAR return signal was governed by

the cyanobacteria populations for the prime reason that the LIDAR signal is more sensitive to larger, irregularly shaped particles. During our field surveys, the largest particles in the waters were dominated by cyanobacteria cells, strands and colonies. Because of the use of the cross-polarized return, water molecules, very small particles, and spherical particles did not contribute to the LIDAR signal. Thus, the abrupt transitions seen in echograms from north-south transects in Areas 2 and 5 make sense when accounting for this view, and is really the only plausible way to interpret the LIDAR data.

Concerning cell identification in the holographic imagery, assumptions had to be made for cell dimensions for the cyanobacteria. *Planktothrix* strands were readily identifiable, but we are not certain of the mean cell length during this bloom event. Our dimensions were based on literature values, but the ultimate impact of this on the error budget for the cell counts is unknown. The same assumptions hold for the *Microcystis* colonies. While readily identifiable, the number of cells per colony was based on reported sizes from the literature. As this was the first field deployment of the HOLOCAM in a freshwater cyanobacteria bloom, the uncertainties of cell counts are not quantified yet for this instrument in this environment.

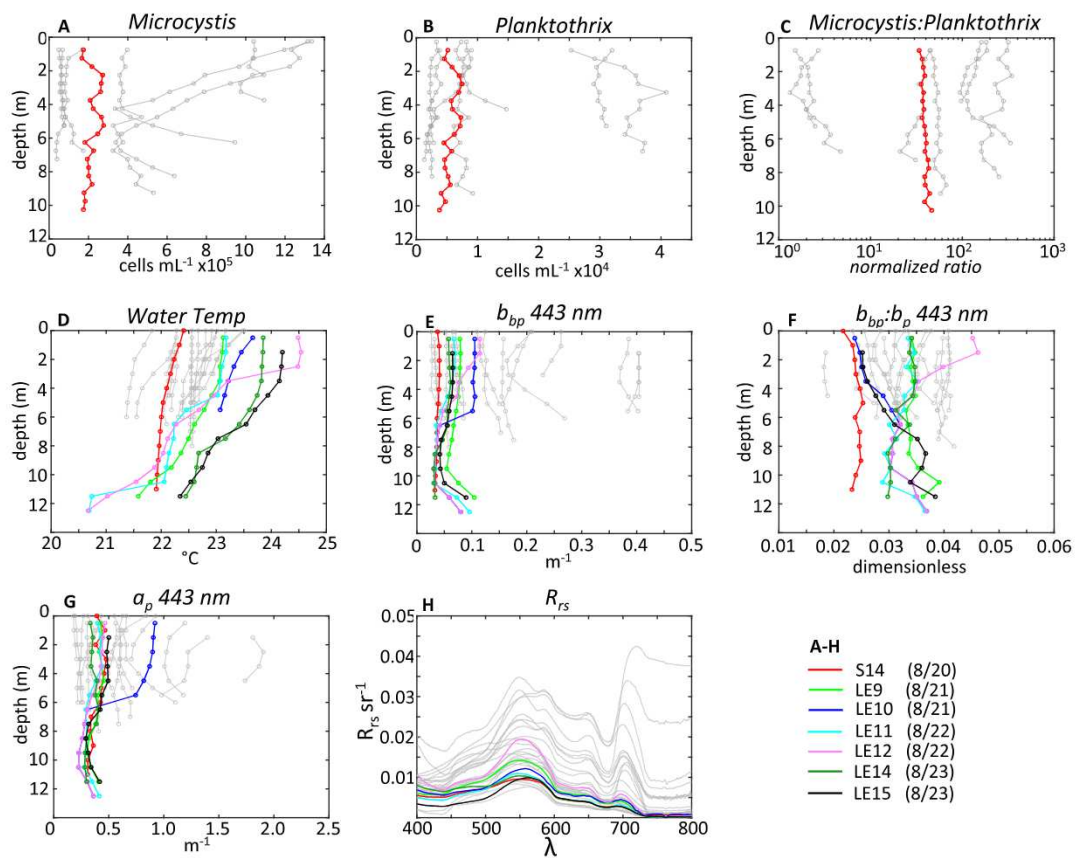


**Fig. 12.** Holographic and IOP vertical profile data are highlighted for stations S14 taken on August 19, 2014 in Area 8. IOP-only profiles for LE9 and LE10 (August 21, 2014), LE11 and LE12 (August 22, 2014), and LE14 and LE15 (August 22, 2014). A: *Microcystis* counts; B: *Planktothrix* counts; C: cell count ratio normalized to column integrated sum for *Planktothrix* and *Microcystis*; D: water temperature; E: particle backscatter at 443 nm; F: particle backscatter ratio at 443 nm; G: particle absorption at 443 nm; H: above-water  $R_{rs}$ . Note: gray lines in plots A through H indicate profiles of all other stations not in the area for comparative visualization.

With these considerations, the correlations provide some metric of confirmation that the LIDAR was detecting the vertical cyanobacteria distribution. The merging of these observations and the IOP profiles, the reflectance measurements and the pigment distributions fit together and form a three-dimensional picture of a multi-species cyanobacteria bloom at peak development.

#### 4.2. Plankton distributions

The two main cyanobacteria genera present in Lake Erie in August of 2014 - *Planktothrix* and *Microcystis* - exhibited different vertical distribution patterns across the lake basins. The *Planktothrix* populations were lower in cell count relative to *Microcystis*, and were found in the southwestern central basin near Sandusky Bay, and the southeastern edge of the western basin. Sandusky Bay directly flows into the southwestern central basin, and is a source of cyanobacteria to Lake Erie. The prominent cyanobacteria species in Sandusky Bay is *Planktothrix agardhii* (Davis et al., 2015; Chaffin and Bridgeman, 2014; Rinta-Kanto and Wilhelm, 2006), which is commonly found in metallimnion layers (Halvstedt et al., 2007) and shallow turbid freshwaters (Scheffer et al., 1997). Sandusky Bay fits this latter description and is an ideal habitat for *Planktothrix agardhii*. In contrast, the optically clearer surface waters of central basin are not ideal for *Planktothrix agardhii*. At the time of our study, it is plausible that as Sandusky Bay waters entered and mixed with the clearer, less turbid waters of the central basin, the *Planktothrix* cells and colonies were exposed to higher light, and maintained a photoprotective strategy through pigment enhancement and descent through the water column by buoyancy regulation until preferred light levels were reached.

The concentrations of *Planktothrix* populations increased with depth

in both western and central basins. In contrast, *Microcystis* cells and colonies were found in abundance near the surface, usually within a few meters. The surface layer exhibited remarkable stability and was a consistent and prominent feature that stretched from Maumee Bay to the islands in an east–west direction and roughly half way across the western basin in a north–south direction. These distributions were observed during a low-wind period, and a near-surface layer roughly 1 m to 2 m thick was present over successive days throughout the week of observation. In this layer, *Microcystis* cells/colonies formed the primary organic component of the surface particle field and were numerically an order of magnitude greater than *Planktothrix* cell counts.

The instances where the two genera co-occurred revealed vertical differentiation by light preferences/tolerances, allowing for co-existence. *Planktothrix* colonies were consistently deeper in the water column than the surface *Microcystis* layer, but depths of the cell maxima varied in relation to light availability. Dense concentrations of near-surface *Microcystis* populations increased light attenuation within the water column, which would explain the shallower position of the *Planktothrix* maxima in these waters. In this context, *Planktothrix* migrated both up and down to depths where light was optimal for their photosynthesis. *Microcystis* was largely absent in the central basin, which not only removes resource competition for *Planktothrix*, but also the light shielding function that *Microcystis* provided in the western basin. Our previous analysis of surface IOPs indicated that the central basin waters had higher relative absorption than the western basin, mostly due to colored dissolved organic matter (Moore et al., 2017). This would provide some additional light shielding for the central basin populations, but not to the degree of dense *Microcystis* surface layers as the attenuation coefficients were higher in western basin compared to the central basin.

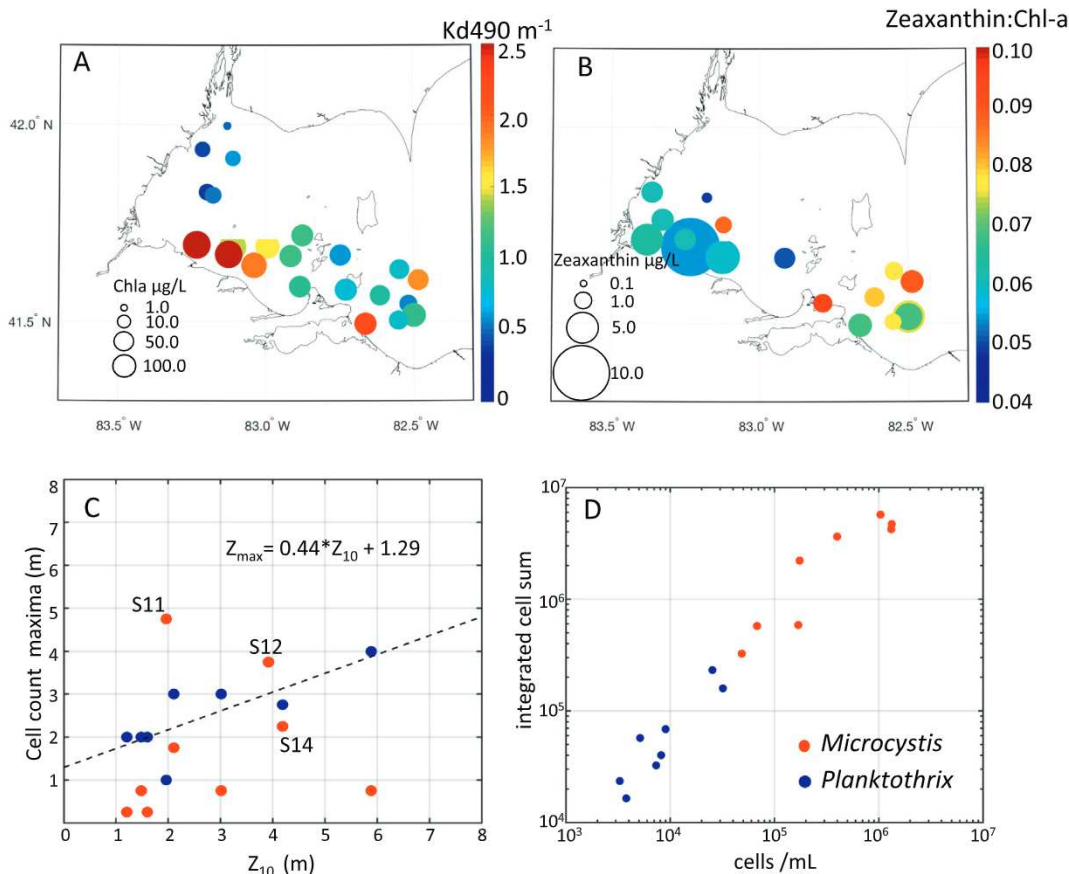


**Fig. 13.** A: Map of *Chl-a* (circle size) color-coded by the attenuation coefficient at 490 nm ( $K_d490$ ); B: map of zeaxanthin (circle size) color-coded by the ratio of zeaxanthin to *Chl-a*; C: depth of *Planktothrix* (blue) and *Microcystis* (red) maximum cell count versus optical depth, line fit to *Planktothrix* only; D: column-integrated cell counts for *Microcystis* and *Planktothrix* versus surface cell count. Stations S11, S12 and S14 showed weak *Microcystis* vertical structure, and positions on graph may not be highly accurate. (For interpretation of the references to color in this figure legend, the reader is referred to the web version of this article.)

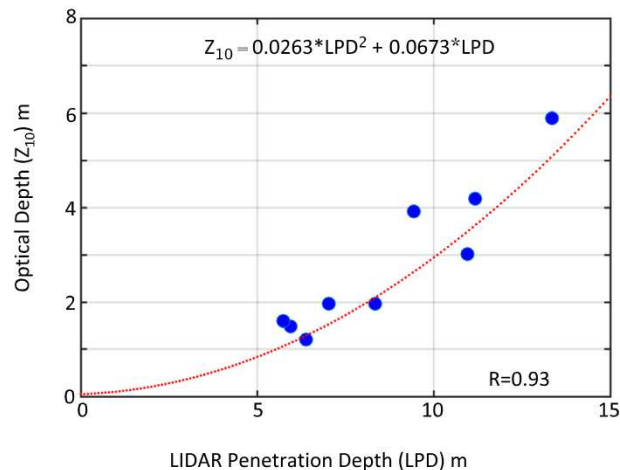


**Fig. 14.** Optical depth at the 10% light level ( $Z_{10}$ ) versus LIDAR penetration depth (LPD) from stations and nearest LIDAR track point shown in Table 5. A quadratic curve was fitted to the data points (red). (For interpretation of the references to color in this figure legend, the reader is referred to the web version of this article.)

A succession of different cyanobacteria species has been previously observed during summer/fall periods in western Lake Erie. Changes in nutrient concentrations (particularly nitrogen) from replete to deplete conditions has been linked to the collapse of *Microcystis* and rise of *Anabaena* communities (Chaffin and Bridgeman, 2014; Michalak et al.,

2013). Although *Microcystis* has been typically found as the dominant species during summer (Stumpf et al., 2012), co-occurrence of multiple cyanobacteria species is not uncommon in Lake Erie (Kutovaya et al., 2012; Millie et al., 2009) and elsewhere (Gitelson, 2017; Gagala et al., 2010; Davis et al., 2003). Morphological and genetic differences may account for resource partitioning. Among these, light is a resource that elicits differential responses by cyanobacteria to its vertical variation in spectral quality and intensity.

Vertical regulation through buoyancy control gives planktonic organisms an advantage on maintaining a position to their light tolerances. The high light tolerance of *Microcystis* is well known (Walsby, 1991) allowing for survival in surface waters, and gives a competitive advantage in certain conditions. The shade-tolerance of *Planktothrix* is also well known (Konopka, 1982), typically resulting in deeper populations to depths depending on the clarity of the overlying waters. In a comparison between depths where *Planktothrix rubescens* populations reached their maxima, the depth occurred deeper in the clearer Lake Zürich (Walsby et al., 2004) than the English lake Blehlem Tarn and was attributed to light intensity (Davis et al., 2003). The interactions between coexisting *Microcystis* and *Planktothrix* are less known, especially in regards to vertical distributions. The patterns of vertical maxima for *Planktothrix* in this study resemble the patterns in these other systems; the depth of the cell maxima varied according to light intensity with deeper depths associated with more transparent overlying waters.

#### 4.3. On the detection of cyanobacteria blooms from remote sensing

One objective of satellite monitoring of cyanobacteria is to

determine water column concentration for water quality assessments (e.g., [Wynne and Stumpf, 2015](#)). Currently, available algorithms do not differentiate between species or genera (e.g., [Hunter et al., 2010](#); [Wynne et al., 2010](#); [Simis et al., 2005](#)). Although lower in cell number by an order of magnitude, the *Planktothrix* population observed in this study was nonetheless an important part of the cyanobacteria community, and was the dominant algal population in the central basin. The lower cell number and more diffuse and deeper distributions challenge the capabilities of detection through passive remote sensing, which center on spectral features that are expressed from 620 nm (PC absorption) through the red/NIR region (high biomass backscatter/absorption).

The  $R_{rs}$  peaks in the red/NIR region have been observed for decades across many freshwater systems (see [Schalles et al., 1998](#) and references therein). In earlier studies, the source of the peaks was not well understood ([Gitelson, 1992](#)), but it was noted early on that spectral variations in the red/NIR, as well as at 620 nm, could be exploited for algorithms to detect cyanobacteria blooms. Since then, a variety of algorithms have been developed to quantify total algal biomass ([Gitelson et al., 2008](#)), cyanobacteria bloom intensity ([Wynne et al., 2010](#)) and floating vegetation ([Hu et al., 2010](#); [Matthews et al., 2012](#)) using reflectance from a combination of red/NIR bands. Early remote sensing studies relied on aircraft imagery ([Dierberg and Carriker, 1994](#)). [Kutser \(2004\)](#) showed the capability of a satellite in observing these spectral features with the Hyperion sensor, a prototype hyperspectral radiometer that extended bands into the red and NIR. However, it was not until the MERIS sensor that a global orbiting satellite was equipped with a channel centered at 709 nm. [Gower et al. \(2005\)](#) was one of the first studies to publish data on the use of the MERIS 709 nm channel for detecting special blooms of phytoplankton. Relations of the peak height (between 680 nm and 750 nm) and *Chl-a* showed tight relationships in various water bodies ([Gower et al., 2005](#)), and has become an important channel for the detection of freshwater cyanobacteria and eutrophic conditions.

[Gitelson \(1992\)](#) and [Schalles et al. \(1998\)](#) attributed the  $R_{rs}$  peak between 700 nm and 710 nm to algal biomass. This peak is governed by the competing processes on the fate of photons between water absorption and particle backscatter ([Kutser et al., 2008](#)). Near-surface particles can overcome water absorption of photons. The overall strength of the  $R_{rs}$  peak is a function of the vertical position of particles, their number and backscatter efficiency. In the case of gas-vacuolate cyanobacteria, the backscatter efficiency is greatly enhanced due to the intracellular gas vacuoles ([Matthews and Bernard, 2013](#) and references therein). The resulting positive buoyancy can position and maintain these cells near the surface, as is often the case with *Microcystis*. Buoyant cyanobacteria near the surface will enhance the red/NIR  $R_{rs}$  features relative to other algal groups because of these traits. [Binding et al. \(2011\)](#) estimated a 3–4 fold increase in  $R_{rs}$  from vertically mixed to a surface concentration of the same population of gas-vacuolate cyanobacteria, also shown in a modeling study by [Kutser et al. \(2008\)](#). However, a sufficient number of cyanobacteria cells in surface waters is needed to impact red/NIR  $R_{rs}$ . While the threshold for number of cells is theoretically lower than other non-vacuolate species because of the higher backscatter, low levels of surface populations of cyanobacteria leave a weak or undistinguished trace on  $R_{rs}$ , as was the case for the central basin open water *Planktothrix* bloom. The degree to which remote sensing can specifically detect cyanobacteria blooms is influenced by the ecology and light tolerances/preferences of species. There are limitations to what remote sensing can provide, as the near-surface communities may be different from deeper populations and column integrated biomass may be far different than what is being detected at the surface.

These red/NIR  $R_{rs}$  characteristics of *Microcystis* blooms are not exclusive. Floating sargassum have been detected in marine environments ([Gower et al., 2006](#)) based on red/NIR  $R_{rs}$  features that are similar to surface scums of cyanobacteria blooms. Other cyanobacteria in

brackish and freshwater also can produce  $R_{rs}$  features similar to *Microcystis* when they are blooming near the surface. [Walsby et al. \(1997\)](#) reported on surface scum formation in the brackish Baltic Sea by the gas-vacuolate cyanobacteria *Aphanizomenon flos-aquae*, and [Shaw et al. \(1999\)](#) reported on thick, brown surface scums of *Aphanizomenon ovalisporum* in Australian lakes. [Binding et al. \(2011\)](#) associated blooms of *Aphanizomenon flos-aquae* with red/NIR features in Lake of the Woods, Minnesota. [Schalles et al. \(1998\)](#) reported similar  $R_{rs}$  features in the red/NIR for blooming *Synechococcus* sp. - a diatom - and *Anabaena* sp. - a cyanobacteria - at different times of year in a eutrophic, freshwater lake. In contrast, low-light adapted *Planktothrix* often dominate in shallow turbid lakes ([Scheffer et al., 1997](#)), but are usually found deeper in the water column in clearer lakes away from where remote sensing can detect their presence ([Davis et al., 2003](#); [Walsby et al., 2004](#)).

The impact of dense, near-surface particles with enhanced backscatter properties (e.g., vacuolate cyanobacteria) on  $R_{rs}(\lambda)$  results in a broad elevation of spectral magnitude, accentuated at certain wavelengths dictated by the interplay of light absorption and scattering. [Kutser \(2004\)](#) examined the depth range of light extinction in the context of near-surface cyanobacteria blooms, and found the optical depth of light ( $Z_{10\%}$ ) decreased from a few meters to zero when cyanobacteria biomass ranged from  $1 \text{ mg/m}^3$  to levels of surface scum in the Baltic Sea. Calculations for  $Z_{10\%}$  from this study were similar, although we note that these are an estimate based on the surface layer. In the Detroit River plume, the optical depths were deepest averaging to 4.67 m. At stations around the islands and in the central basin, optical depths ranged from 1.2 m to 4.2 m averaging to 2.80 m. Stations in the western basin with *Microcystis* were shallowest ranging from 0.84 m to 2.10 m and an average of 1.4 m. In the case of *Microcystis* with near-surface populations occupying the top 2 m, 90% of photons reaching the satellites leaving from the water originate from the about the first meter or less. As a consequence, biomass estimates based on passive remote sensing data can miss a major fraction of the microbial community, as the penetration depth is a function of the particle density and associated optical clarity of the water column. The LIDAR showed a deeper penetration of light and ability to resolve a greater vertical range for determining particle distributions. The LIDAR penetrations depths were highly correlated with the optical depth. These results seem to favor the use LIDAR technology for assessing the particle distribution and concentrations over passive remote sensing, even in a highly turbid environment such as Lake Erie.

## 5. Conclusions

The combination of active and passive remote sensing measurements with *in situ* profiles of optical properties and cell counts generated a three-dimensional view of the particle distributions highlighting horizontal and vertical distributions of gas-vacuolate cyanobacteria. An advantage of LIDAR measurements is the deeper and finer resolution of the vertical particle distribution relative to passive 'ocean color' sensors. Despite time and space differences in matchup quality, the LIDAR-derived vertical particle structure was explained by cyanobacteria cell counts determined with a profiling holographic digital system. Based on these results, additional studies that specifically coordinate LIDAR with *in situ* optical and holographic measurements would improve the quantitative uses of LIDAR data. In this study, we used the LIDAR data in a qualitative way to describe overall particles distributions across a large lake area. We believe the cyanobacteria populations that comprised the particle fields were well described by these observations, which could be applied to other systems. However, deeper lakes with sub-surface populations may be more problematic as there are limitations to the penetration of a LIDAR system. The use of holography was also important to understanding these vertical distributions in terms of particle composition. The holographic system used in this study was capable of observing the particles undisturbed, as there was no

pumping of water into camera fields which minimized cell/c colony disruption. The system detects particles over a large size range, from several microns to several millimeters. Given the large colony and aggregate sizes that cyanobacteria can form, this system is well suited for enumerating and identifying cyanobacteria genera in these types of waters and conditions.

From a macroscopic point of view, the cyanobacteria formed one large bloom, but details of the data set reveal two co-occurring populations - *Microcystis* and *Planktothrix*. Dense *Microcystis* populations were concentrated near the surface and increased light attenuation, while *Planktothrix* populations were more diffuse, and showed variable vertical maxima depending on the degree of surface light attenuation. These preferences may allow for a degree of niche partitioning and co-existence. *Microcystis* cell counts were an order of magnitude higher than counts for *Planktothrix*, although the latter was dominant in the southwestern central basin.

We have shown that the cyanobacteria bloom in western Lake Erie comprised two different genera and have linked their distributions to light tolerances/preferences. However, we know less about other ecological aspects, such as cell sources, nutrient sources and life stages. We do not know what part of either populations were ascending or descending, or to what degree nutrient competition was playing a role in these distributions, if at all. We do not have a lot of detail on the vertical distributions of toxins. However, the information we have collated presents a unique picture for understanding how these two cyanobacteria genera co-exist along a light gradient.

These ecological life attributes have impacts on the light field relevant to passive remote sensing. Detecting and quantifying cyanobacteria from remote sensing and bio-optical algorithms that exploit red/NIR features have limitations that are dependent on the vertical distribution and concentrations of the cells. When high amounts of cells are concentrated near or at the surface, the signal is more pronounced and detection is more reliable than diffusely distributed populations. This would favor more reliable detection of *Microcystis* compared to *Planktothrix*. We can now add a fourth state to the three defined by Kutser (2004) - a sub-surface vertically varying population with non-homogenous structure. This state could encompass a range of vertical shapes. These states could switch from one to another rapidly, within the span of hours, depending on external conditions (e.g., wind, solar irradiation), without changing the column population and overall column community. There is a continuum of optical outcomes from many permutations of cell density, vertical position, species composition, and pigment content - all which determine light reflectance. There are likely constrained ranges of optical outcomes though within each state apart from the whole, and defining these ranges and linking them to these states would be beneficial towards connecting remote sensing data to cyanobacteria distributions and associated water quality indices.

### Conflict of interest statement

The authors declare no conflict of interest. Copyright permission has been obtained for re-production of Fig. 3 from the copyright holders.

### Author contributions

TM, JS, MT and SR designed the main field study for the UNH data set. TM, JS, MT, and NS acquired the field data. JC collected and processed the LIDAR data. SR provided the logistical use of NOAA lab space for instrument assembly and water sample processing, use of the NOAA R/V for the study and field support. TJ, JS, MT, AN and MM processed and analyzed the discrete water samples. AN processed the HOLOCAM imagery for cell and particles counts and concentrations. TM and JS made the radiometric measurements. JS, MT and NS processed and analyzed the IOP data. All authors contributed to, commented on and edited the paper.

### Funding

Funding for TM, MT, and JS was provided by the National Science Foundation (OCE-1313783) and the National Institute for Environmental Health Sciences (1R01ES021929-01). JC was partially supported by the Naval Research Laboratory (N001735IP00017). The Naval Research Laboratory also paid aircraft costs. Funding support for NRLSSC components of this research was provided through the Office of Naval Research (Program element 0601153N) and the Center for Advancement of Science in Space (RFI No. CASIS 2012-3). Additional support for MT was also provided through a Harbor Branch Institute of Oceanography Foundation award, and NASA grants NNX15AR65G and NNX15AN17G. Additional support for JS, MM and AN was provided by the Harbor Branch Oceanographic Institute Foundation, NASA (NNX15AR65G) and NSF (1634053, 1657332). Funding support for TJ and SR was provided through the Great Lakes Restoration Initiative. This manuscript is contribution number 1137 for the Cooperative Institute for Great Lakes Research, University of Michigan. This manuscript is NOAA Great Lakes Environmental Research Laboratory contribution No. 1913.

### Acknowledgments

We would like to thank the captains of the NOAA GLERL ships used for this study. Aircraft altitude data were supplied by David Miller of the U.S. Naval Research Laboratory. We thank Colleen Mouw for chlorophyll data contributed for Figure 4. We thank Heidi Dierssen for the use of the ASD radiometer used to collect radiometry measurements. We thank Audrey Ciochetto, Angela Hu, Danna Palladino, Steve Constant and Kyle Beadle for field support. We also thank the three anonymous reviewers and the editors at Remote Sensing of Environment.

### Appendix A. Supplementary data

Supplementary data to this article can be found online at <https://doi.org/10.1016/j.rse.2019.02.025>.

### References

- APHA, 1998. Standard Methods for the Examination of Water and Waste Water. American Public Health Association, Washington, D.C.
- Austin, R., 1972. The remote sensing of spectral radiance from below the ocean surface. In: Jerlov, N., Nielsen, S. (Eds.), Optical Aspects of Oceanography. Academic, New York, pp. 201–213.
- Binding, C., Greenberg, T., Berome, J., Bukata, R., Letourneau, G., 2011. An assessment of MERIS algal products during an intense bloom in Lake of the Woods. Journal of Plankton Research 33, 793–806. <https://doi.org/10.1093/plankt/fbq133>.
- Blank, C., 2013. Origin and early evolution of photosynthetic eukaryotes in freshwater environments: reinterpreting proterozoic paleobiology and biogeochemical processes in light of trait evolution. Journal of Phycology 130, 243–253. <https://doi.org/10.1111/jpy.12111>.
- Carder, K., Steward, R., 1985. A remote-sensing reflectance model of a red tide dinoflagellate off West Florida. Limnology and Oceanography 30, 286–298.
- Carey, C., Ibelings, B., Hoffman, E., Hamilton, D., Brookes, J., 2012. Eco-physiological adaptations that favour freshwater cyanobacteria in a changing climate. Water Research 46, 1394–1407.
- Chaffin, J., Bridgeman, T., 2014. Organic and inorganic nitrogen utilization by nitrogen-stressed cyanobacteria during bloom conditions. Journal of Applied Phycology 26, 299–309. <https://doi.org/10.1007/s10811-013-0118-0>.
- Churnside, J., 2014. Review of profiling oceanographic lidar. Optical Engineering 53, 051405. <https://doi.org/10.1117/1.OE.53.5.051405>.
- Churnside, J., 2015. Subsurface plankton layers in the Arctic Ocean. Geophysical Research Letters 42, 4896–4902. <https://doi.org/10.1002/2015GL064503>.
- Churnside, J., Donaghay, P., 2009. Thin scattering layers observed by airborne lidar. ICES Journal of Marine Science 66, 778–789. <https://doi.org/10.1093/icesjms/fsp029>.
- Churnside, J., Marchbanks, R., Lembke, C., Beckler, J., 2017. Optical backscattering measured by airborne lidar and underwater glider. Remote Sensing 9, 379. <https://doi.org/10.3390/rs9040379>.
- Churnside, J., Sharov, A., Richter, R., 2011. Aerial surveys of fish in estuaries: a case study in Chesapeake Bay. ICES Journal of Marine Science 68, 239–244. <https://doi.org/10.1093/icesjms/fsq138>.
- Churro, C., Azevedo, J., Vasconcelos, V., Silva, A., 2017. Detection of a *Planktothrix*

*agardhii* bloom in Portuguese marine coastal waters. *Toxins* 9, 391.

Davis, P., Dent, M., Parker, J., Reynolds, C., Walsby, A., 2003. The annual cycle of growth rate and biomass change in *Planktothrix* spp. in Blelham Tarn, English Lake District. *Freshwater Biology* 48, 852–867.

Davis, T., Bullerjahn, G., Tuttle, T., McKay, R., Watson, S., 2015. Effects of increasing nitrogen and phosphorus concentrations on phytoplankton community growth and toxicity during *Planktothrix* blooms in Sandusky Bay, Lake Erie. *Environmental Science and Technology* 49, 7197–7207.

Desy, J.-P., Sarmento, H., Higgins, H., 2009. Variability of phytoplankton pigment ratios across aquatic environments. *European Journal of Phycology* 44, 319–330.

Dierberg, F., Carrlker, N., 1994. Field testing two instruments for remotely sensing water quality in the Tennessee valley. *Environmental Science and Technology* 28, 16–25.

Gagala, I., Izidorczyk, K., Skowron, A., Kamecka-Plaskota, D., Stefaniak, K., Kokociński, M., Mankiewicz-Boczek, J., 2010. Appearance of toxicogenic cyanobacteria in two Polish lakes dominated by *Microcystis aeruginosa* and *Planktothrix agardhii* and environmental factors influence. *Ecohydrology and Hydrobiology* 10, 25–34. <https://doi.org/10.2478/v10104-009-0045-5>.

Gitelson, A., 1992. The peak near 700 nm on radiance spectra of algae and water: relationships of its magnitude and position with chlorophyll concentration. *International Journal of Remote Sensing* 13, 3367–3373.

Gitelson, A., 2017. Unusual cohabitation and competition between *Planktothrix rubescens* and *Microcystis* sp. (cyanobacteria) in a subtropical reservoir (Hammam Debagh) located in Algeria. *PLOS ONE* 13, 3367–3373. <https://doi.org/10.1371/journal.pone.0183540>.

Gitelson, A., Dall'Olmo, G., Moses, W., Rundquist, D., Barrow, T., Fisher, T., Gurlin, D., Holz, J., 2008. A simple semi-analytical model for remote estimation of chlorophyll-a in turbid waters: validation. *Remote Sensing of Environment* 112, 3582–3593.

Gould, R., 2014. [https://seabass.gsfc.nasa.gov/archive/NRL/Lake\\_Erie\\_Aug.2014/rv\\_muksie/documents](https://seabass.gsfc.nasa.gov/archive/NRL/Lake_Erie_Aug.2014/rv_muksie/documents). NASA SeaWiFS Bio-optical Storage System (SeaBASS).

Gower, J., Hu, C., Borstad, G., King, S., 2006. Ocean color satellites show extensive lines of floating sargassum in the Gulf of Mexico. *IEEE Trans. Geosci. Remote Sens.* 44, 3619–3625.

Gower, J., King, S., Borstad, G., Brown, L., 2005. Detection of intense plankton blooms using the 709 nm band of the MERIS imaging spectrometer. *International Journal of Remote Sensing* 26, 2005–2012.

Halvstedi, C., Rohrlack, T., Andersen, T., Skulberg, O., Evardsen, B., 2007. Seasonal dynamics and depth distribution of *Planktothrix* spp. in Lake Steinsfjorden (Norway) related to environmental factors. *Journal of Plankton Research* 29, 471–482.

Harke, M., Steffen, M., Gobler, C., Otten, T., Wilhelm, S., Wood, S., Paerl, H., 2016. A review of the global ecology, genomics, and biogeography of the toxic cyanobacterium, *Microcystis* spp. *Harmful Algae* 54, 4–20.

Heukelem, L.V., Thomas, C., 2001. Computer-assisted high-performance liquid chromatography method development with applications to the isolation and analysis of phytoplankton pigments. *Journal of Chromatography A* 910, 31–49.

Hu, C., Lee, Z., Ma, R., Yu, K., Li, D., Shang, S., 2010. Moderate resolution imaging spectroradiometer (MODIS) observations of cyanobacteria blooms in Taihu Lake, China. *Journal of Geophysical Research* 115. <https://doi.org/10.1029/2009JC005511>.

Humphries, S., Lyne, V., 1988. Cyanophyte blooms: the role of cell buoyancy. *Limnology and Oceanography* 33, 79–91.

Hunter, P., Tyler, A., Carvalho, L., Codd, G., Maberly, S., 2010. Hyperspectral remote sensing of cyanobacterial pigments as indicators for cell populations and toxins in eutrophic lakes. *Remote Sensing of Environment* 114, 2705–2718.

Ibelings, B., Kroon, B., Mur, C., 1994. Acclimation of photosystem II in a cyanobacterium and a eukaryotic green alga to high and fluctuating photosynthetic photon flux densities, simulating light regimes induced by mixing in lakes. *New Phytologist* 128, 407–424.

IJC, 2014. A balanced diet for Lake Erie: reducing phosphorus loadings and harmful algal blooms. ISBN: 978-1-927336-07-6.

Jeffrey, S., Mantoura, R., 78, S.W.G., Wright, S., Staff, U., of Scientific Unions. Scientific Committee on Oceanic Research, I.C., Unesco, 1997. *Phytoplankton Pigments in Oceanography: Guidelines to Modern Methods. Monographs on Oceanographic Methodology* UNESCO Publishing9789231032752.

Joosse, P., Baker, D., 2011. Context for re-evaluating agricultural source phosphorus loadings to the Great Lakes. *Canadian Journal of Soil Science* 91, 317–327.

Joung, S.-H., Kim, C.-J., Ahn, C.-Y., Jang, K.-Y., Boo, S., Oh, H.-M., 2006. Simple method for a cell count of the colonial cyanobacterium, *Microcystis* sp. *The Journal of Microbiology* 44, 562–565.

Kane, D., Conroy, J., Richards, R., Baker, D., Culver, D., 2014. Re-eutrophication of Lake Erie: correlations between tributary nutrient loads and phytoplankton biomass. *Journal of Great Lakes Research* 40, 496–501.

Katz, J., Sheng, J., 2010. Applications of holography in fluid mechanics and particle dynamics. *Annu. Rev. Fluid Mech.* 42, 531–555. <https://doi.org/10.1146/annurev-fluid-121108-145508>.

Kirk, J., 1994. *Light and Photosynthesis in Aquatic Ecosystems*. Cambridge University Press, Cambridge, England.

Kokociński, M., Stefaniak, K., Mankiewicz-Boczek, J., Izidorczyk, K., Soiniemi, J., 2010. The ecology of the invasive cyanobacterium *Cylindrospermopsis raciborskii* (Nostocales, Cyanophyta) in two hypereutrophic lakes dominated by *Planktothrix agardhii* (Oscillatoriaceae, Cyanophyta). *European Journal of Phycology* 45, 365–374. <https://doi.org/10.1080/09670262.2010.492916>.

Konopka, A., 1982. Buoyancy regulation and vertical migration by *Oscillatoria rubescens* in Crooked Lake, Indiana. *British Phycological Journal* 17, 427–442. <https://doi.org/10.1080/00071618200650451>.

Konopka, A., 1989. Metalimnetic cyanobacteria in hard-water lakes: buoyancy regulation and physiological state. *Limnology and Oceanography* 34, 1174–1184.

Kromkamp, J., Walsby, A., 1990. A computer model of buoyancy and vertical migration in cyanobacteria. *Journal of Plankton Research* 12, 161–183.

Kutovaya, O., McKay, R., Beall, B., Wilhelm, S., Kane, D., Chaffin, J., Bridgeman, T., Bullerjahn, G., 2012. Evidence against fluvial seeding of recurrent toxic blooms of *Microcystis* spp. in Lake Erie's western basin. *Harmful Algae* 15, 71–77. <https://doi.org/10.1016/j.hal.2011.11.007>.

Kutser, T., 2004. Quantitative detection of chlorophyll in cyanobacterial blooms by satellite remote sensing. *Limnology and Oceanography* 49, 2179–2189.

Kutser, T., Metsamaa, L., Dekker, A., 2008. Influence of the vertical distribution of cyanobacteria in the water column on the remote sensing signal. *Estuarine, Coastal and Shelf Science* 78, 649–654.

Lee, J., Churnside, J., Marchbanks, R., Donaghay, P., Sullivan, J., 2013. Oceanographic lidar profiles compared with estimates from in situ optical measurements. *Appl. Opt.* 52, 786–794. <https://doi.org/10.1364/AO.52.000786>.

Lee, Z.-P., Du, K.-P., Arnone, R., 2005. A model for the diffuse attenuation coefficient of downwelling irradiance. *Journal of Geophysical Research* 110. <https://doi.org/10.1029/2004JC002275>.

Matthews, M., Bernard, S., 2013. Using a two-layered sphere model to investigate the impact of gas vacuoles on the inherent optical properties of *Microcystis aeruginosa*. *Biogeosciences* 10, 8139–8157. <https://doi.org/10.5194/bg-10-8139-2013>.

Matthews, M., Bernard, S., Robertson, L., 2012. An algorithm for detecting trophic status (chlorophyll-a), cyanobacterial-dominance, surface scums and floating vegetation in inland and coastal waters. *Remote Sensing of Environment* 124, 637–652.

Metsamaa, L., Kutser, T., Strombeck, N., 2006. Recognizing cyanobacteria blooms based on their optical signature: a modelling study. *Boreal Environment Research* 11, 493–506.

Michalak, A., Anderson, E., Beletsky, D., Boland, S., Bosch, N., Bridgeman, T., et al., 2013. Record-setting algal bloom in lake erie caused by agricultural and meteorological trends consistent with future conditions. *Proceedings of the National Academy of Sciences*. <https://doi.org/10.1073/pnas.1216006110>.

Millie, D., Fahnstiel, G., Dyble-Bressie, J., Pigg, R., Rediske, R., Klarer, D., Tester, P., Whitaker, R., 2009. Late-summer phytoplankton in western Lake Erie (Laurentian Great Lakes): bloom distributions, toxicity, and environmental influences. *Aquatic Ecology* 43, 915–934. <https://doi.org/10.1007/s10452-009-9238-7>.

Moore, T., Mouw, C., Sullivan, J., Twardowski, M., Burtner, A., Ciochetto, A., McFarland, M., Nayak, A., Paladino, D., Stockley, N., Johengen, T., Yu, A., Ruberg, S., Weidemann, A., 2017. Bio-optical properties of cyanobacteria blooms in western Lake Erie. *Frontiers in Marine Science* 4:300. <https://doi.org/10.3389/fmars.2017.00300>.

Mueller, J., Fargion, G., McClain, C., 2003. *Ocean Optics Protocols for Satellite Ocean Color Sensor Validation, Revision 4, Volume IV*. National Aeronautical and Space Administration, Goddard Space Flight Space Center, Greenbelt, Maryland.

Nayak, A., McFarland, M., Sullivan, J., Twardowski, M., 2018. Evidence of ubiquitous preferential particle orientation in representative oceanic shear flows. *Limnology and Oceanography* 63, 122–143.

Oliver, R., 1994. Floating and sinking in gas-vacuolate cyanobacteria. *Journal of Phycology* 30, 161–173.

Oliver, R., Walsby, A., 1984. Direct evidence for the role of light-mediated gas vesicle collapse in the buoyancy regulation of *Anabaena flos-aquae* (cyanobacteria). *Limnology and Oceanography* 29, 879–886.

Paerl, H., Bland, P., Bowles, D., Haibach, M., 1985. Adaptation to high-intensity, low-wavelength light among surface blooms of the cyanobacterium *Microcystis aeruginosa*. *Applied and Environmental Microbiology* 49, 1046–1052.

Paerl, H., Otten, T., 2013. Blooms bite the hand that feeds them. *Science* 342, 433–434.

Paerl, H., Tucker, J., Bland, P., 1983. Carotenoid enhancement and its role in maintaining blue-green algal (*Microcystis aeruginosa*) surface blooms. *Limnology and Oceanography* 28, 847–857.

Rinta-Kanto, J., Wilhelm, S., 2006. Diversity of microcystin-producing cyanobacteria in spatially isolated regions of lake erie. *Applied and Environmental Microbiology* 72, 5083–5085. <https://doi.org/10.1128/AEM.00312-06>.

Sánchez-Baracaldo, P., Hayes, P., Blank, C., 2005. Morphological and habitat evolution in the cyanobacteria using a compartmentalization approach. *Geobiology* 3, 145–165.

Schagerl, M., Müller, B., 2006. Acclimation of chlorophyll a and carotenoid levels to different irradiances in four freshwater cyanobacteria. *Journal of Plant Physiology* 163, 709–716.

Schalles, J., Gitelson, A., Yacobi, Y., Kroenke, A., 1998. Estimation of chlorophyll a from time series measurements of high spectral resolution reflectance in an eutrophic lake. *Journal of Phycology* 34, 383–390.

Scheffer, M., Rinaldi, S., Gragnani, A., Mur, L., Nes, E.V., 1997. On the dominance of filamentous cyanobacteria in shallow, turbid lakes. *Ecology* 78, 272–282.

Schlüter, L., Lauridsen, T., Krogh, G., Jørgensen, T., 2006. Identification and quantification of phytoplankton groups in lakes using new pigment ratios – a comparison between pigment analysis by hplc and microscopy. *Freshwater Biology* 51, 1474–1485.

Shaw, G., Sukenik, A., Livne, A., Chiswell, R., Smith, M., Seawright, A., Norris, R., Eaglesham, G., Moore, M., 1999. Blooms of the cylindrospermopsin containing cyanobacterium, *Aphanizomenon ovalisporum* (Forti), in newly constructed lakes, Queensland, Australia. *Environmental Toxicology* 14, 167–177.

Simis, S., Peeters, S., Gons, H., 2005. Remote sensing of the cyanobacterial pigment phycocyanin in turbid inland water. *Limnology and Oceanography* 50, 237–245.

Stomp, M., Huisman, J., Vordos, L., Pick, F., Laamanen, M., Haverkamp, T., Stal, L., 2007. Colourful coexistence of red and green picocyanobacteria in lakes and seas. *Ecology Letters* 10, 290–298. <https://doi.org/10.1111/j.1461-0248.2007.01026.x>.

Stumpf, R., Wynne, T., Baker, D., Fahnstiel, G., 2012. Interannual variability of cyanobacterial blooms in Lake Erie. *PLOS ONE* 7. <https://doi.org/10.1371/journal.pone.0042444>.

Talapatra, S., Hong, J., McFarland, M., Nayak, A., Zhang, C., Katz, J., Sullivan, J., Twardowski, M., Rines, J., Donaghay, P., 2013. Characterization of biophysical interactions in the water column using *in situ* digital holography. *Marine Ecology Progress Series* 473, 29–51.

Twardowski, M., Sullivan, J., Dalgeish, F., 2016. Novel technologies to study undisturbed particle fields in the ocean. *Sea Technology* 57, 15–19.

Twardowski, M., Sullivan, J., Donaghay, P., Zaneveld, J., 1999. Microscale quantification of the absorption by dissolved and particulate material in coastal waters with an ac-9. *J. Atmos. Ocean. Technol.* 16, 691–707.

Uyeda, J., Harmon, L., Blank, C., 2016. A comprehensive study of cyanobacterial morphological and ecological evolutionary dynamics through deep geologic time. *PLoS One* 11. <https://doi.org/10.1371/journal.pone.0162539>.

Visser, P., Passarge, J., Mur, L., 1997. Modelling vertical migration of the cyanobacterium *Microcystis*. *Hydrobiologia* 349, 99–109.

Walsby, A., 1991. The mechanical properties of the *Microcystis* gas vesicle. *Journal of General Microbiology* 137, 2401–2408.

Walsby, A., 1994. Gas vesicles. *Microbiological Reviews* 58, 94–144.

Walsby, A., Booker, M., 1980. Changes in buoyancy of a planktonic blue-green alga in response to light intensity. *British Phycological Journal* 15, 311–319. <https://doi.org/10.1080/00071618000650321>.

Walsby, A., Hayes, P., Boje, R., Stal, L., 1997. The selective advantage of buoyancy provided by gas vesicles for planktonic cyanobacteria in the Baltic Sea. *New Phytologist* 136, 407–417.

Walsby, A., Ng, G., Dunn, C., Davis, P., 2004. Comparison of the depth where *Planktothrix rubescens* stratifies and the depth where the daily insolation supports its neutral buoyancy. *New Phytologist* 162, 133–145. <https://doi.org/10.1111/j.1469-8137.2004.01020.x>.

Wynne, T., Stumpf, R., 2015. Spatial and temporal patterns in the seasonal distribution of toxic cyanobacteria in western Lake Erie from 2002–2014. *Toxins* 7, 1649–1663.

Wynne, T., Stumpf, R., Tomlinson, M., Dyble, J., 2010. Characterizing a cyanobacterial bloom in western Lake Erie using satellite imagery and meteorological data. *Limnology and Oceanography* 55, 2025–2036.

Xue, K., Zhang, Y., Ma, R., Duan, H., 2017. An approach to correct the effects of phytoplankton vertical nonuniform distribution on remote sensing reflectance of cyanobacterial bloom waters. *Limnology and Oceanography: Methods* 15, 302–319. <https://doi.org/10.1002/lom3.10158>.

Zamankhan, H., Westrick, J., Anscombe, F., Stumpf, R., Wynne, T., Sullivan, J., Twardowski, M., Moore, T., Choi, H., 2016. Sustainable Water Management and Technologies. Taylor and Francis Group, Boca Raton, FL, chap. Chapter 3: sustainable monitoring of algal blooms.

Zaneveld, J., Kitchen, J., Moore, C., 1994. The scattering error correction of reflecting tube absorption meters. *Ocean Optics XII, Proc. SPIE* 2258, 44–55.